SIMULATIONS AND PROTOTYPING OF AN MPGD AND A WIRE-BASED DETECTOR

A Project Report Submitted
in Partial Fulfilment of the Requirements
for the Degree of

MASTER OF SCIENCE

by

S Danush

To

National Institute of Science Education and Research (NISER).

At - Bhimpur, Padanpur, PO - Jatani,

Dist - Khordha – 752050, Odisha, India

DECLARATION

I, along with my undersigned Guide, are co-owners of the copyright of this thesis/dissertation. NISER is hereby granted, exclusive, royalty-free, and non-transferable rights to make available, in full or in part without any modification, this thesis/dissertation in electronic/printed form solely for academic use at no charge. Any use of material from this thesis/dissertation must be accompanied with appropriate citation and prior permission. This thesis/dissertation is not covered under creative commons license.

Date: **Signature of Student**

The thesis work reported in the thesis entitled "..... ....." was carried out under my supervision, in the school of ..... at NISER, Bhubaneswar, India.

Signature of Thesis Supervisor

School:

Date:

ACKNOWLEDGEMENTS

My first thanks go to Prof. Bedangadas Mohanty for providing me the opportunity to work under his guidance on this project and for teaching me a lot of things in science and life in general. I could not have asked for a better guide and mentor for this project.

I thank Dr. Varchaswi K S Kashyap and Dr. Shuddha Shankar Dasgupta for their guidance and for bearing a lot of my amateur doubts I have asked during these past couple of months.

I would like to extend my thanks to the Robotics lab, Dr. Shubankar Mishra, Mr. Jyothish Kumar, Mr. Oommen P Jose, and Mr. Shriman Keshri for letting us use the 3D printer and for getting the prints done during odd hours. I thank Mr. Subasha Rout for his help with electronics and the mechanical engineering tasks we were involved in. His experience and knowledge with circuits are extraordinary.

I thank Dr. Ganesh Jagannath Tambave, Dr. Raveendrababu Karnam, Mr. Ashish Pandav (one of those lakh guldastas), Mr. Debasish Mallick, Mr. Dukhishyam Mallick, Ms. Mouli Chaudhuri, Mr. Prottay Das, Mr. Sudipta Das, and Ms. Swati Saha for making the lab environment memorable, and I proudly say this, the best amongst all of SPS.

I would like to thank Ms. Adishree M, Mr. Akilan K, Mr. Aman Upadhyay, Mr. Chinmay Routray, and Mr. Nisarg Vyas for all the cherishable conversations and for bearing my attitude when deadlines were looming over.

I finally am grateful to my parents and sister for the patience and ever-showering love during all the times I hadn't called them.

ABSTRACT

Gas detectors form an important part of a larger detector in experiments at facilities like those at the Large Hadron Collider (LHC) and Relativistic Heavy Ion Collider (RHIC). There are also applications in fields like medical imaging, and thus an understanding of such devices can help improve science's impact on society. With the invention of the Geiger-Muller counter, the development of gas detectors has come a long way in terms of better design and capabilities. One such detector is the Thick-GEM detector, around which most of this thesis is focused upon. This project involves studying the interaction of radiation and particles with matter, concepts that are crucial to understanding the science behind gas detectors. We then designed and fabricated the Thick-GEM detector and the proportional counter. Tests and experiments with these detectors were conducted, and finally, some simulations using Garfield++ and the neBEM library were done to get more insight into the working principles of these detectors.

Contents

List of Figures

List of Tables

Chapter 1

Outline

This thesis has been divided into four chapters. Chapter 2 discusses the study of energy loss of particles that traverses through matter. These are concepts that are employed and taken advantage of by detectors in most High Energy Physics experiments. The chapter then goes into some pre-requisites to understand the microscopic processes that occur in gaseous detectors. Chapter 3 introduces the history of gaseous detectors, the need for such detectors, and some details on GEMs and Thick-GEMs. We try to capture how the journey of the development of gas detectors brought us to where we are now with new detectors like the Thick-GEM detector. Chapter 4 describes the design and fabrication process of the Thick-GEM detector, with efforts taken to create the entire detector from parts made in India. We then discuss the tests that were conducted to check and run the detector, their subsequent results, and a discussion on a new redesign of the setup. Chapter 5 discusses the fabrication process of the proportional counter, the tests conducted, and subsequent results. Finally, Chapter 6 concludes this thesis.

Chapter 2

Energy Loss of Particles in Matter

A crucial objective in most nuclear or particle physics experiments is the detection of radiation and particles. It is thus essential to look at how different particles and radiation interact with matter. These interactions can be classified into two types based on whether the incident particle is a photon or a charged particle. Information like the energy and position of an incoming particle can be extracted based on information we obtain from these interactions.

2.1 Interaction of Charged Particles With Matter

A charged particle traversing through matter can be characterized by the following interactions it can undergo with the atoms/molecules of the medium [12]:

1. Inelastic collisions with atomic electrons of the medium
2. Elastic scattering with the nuclei of the medium
3. Emission of Cherenkov radiation
4. Nuclear reactions
5. Bremsstrahlung

As explained in [12], inelastic collisions with electrons of the medium and the incident particle involve the excitation or ionization of these electrons, and although the energy lost by the incident particle is not a lot for one such collision, it adds up to a considerable number in the end, because of the total number of such collisions that usually take place. Elastic collisions with the nuclei of the medium do not take place as often as inelastic collisions with the electrons of the medium, and these types of collisions do not account for the majority of energy loss of the incident particle. The other three effects also are possible but are less frequent than the first two.

It is useful to calculate the amount of energy lost by an incoming particle as it traverses through a medium, and it was the seminal work of Niels Bohr, Hans Bethe, and Felix Bloch, among others, that paved the way for these calculations. The information from these calculations formed the foundations based on which we

built detectors that can now help us identify the (charged) particle and calculate the energy with which they hit the detector. Although Bohr derived the stopping power (mean energy lost per unit path length) for heavy charged particles using classical arguments, it was Bethe and Bloch that performed the same using quantum mechanics. The derivation by Bohr is explained in Appendix A.1.

The Bethe-Bloch equation describes the energy loss (through many interactions) that heavy-charged particles like alpha particles undergo while traversing through a medium. The equation is as follows:

$$-\frac{dE}{dx} = 2\pi N_{\mathrm{a}} r_{\mathrm{e}}^2 m_{\mathrm{e}} c^2 \rho \frac{Z}{A} \frac{z^2}{\beta^2} \left[\ln\left(\frac{2m_e \gamma^2 v^2 W_{\max}}{I^2} \right) - 2\beta^2 - \delta - 2\frac{C}{Z} \right], \tag{2.1}$$

where r_e and m_e are the radius and mass of an electron respectively, N_a is the Avogadro's number, I is the mean excitation potential, Z, A, and ρ are the atomic number, atomic weight, and density of the medium respectively, z and v are the charge and velocity of the incident particle respectively, δ and C are the density and shell correction terms respectively and $W_{\max}$ is the maximum energy transfer possible in a single collision (obtained from kinematics).

The expressions obtained by Bohr and Bethe-Bloch arise from classical and quantum mechanical frameworks, respectively. However, it is also to be noted that apart from the correction terms, the final equations have the same dependence on z, Z, A, ρ, and differ in v by one degree. (Here, degree means the power of the variable. Eg. - degree of x in x^3 is 3.) Bohr's result is pretty accurate, considering it was derived from a classical picture.

The density correction term is required to deal with the polarisation that the incident particle can bring about in the atoms of the medium along its path. Due to this, the electrons further away from this path will experience a shielding from the true electric field intensity of the incident particle. The Bethe-Bloch equation would break down if the velocity of the incident particle is comparable to or lower than the orbital velocity of the bound electrons of the atoms of the medium. This is because the equation assumes that the electrons of the medium are stationary with respect to the incident particle. The shell corrections precisely look into this aspect. It accounts for effects that arise when the velocity of the incident particle is low.

We see that the Bethe-Bloch equation is initially dominated by the β^2 term, so there is a drop in $\mathrm{d}E/\mathrm{d}x$ as the energy of the incident particle increases. At higher energies, the logarithmic term starts to weigh in, thus increasing $\mathrm{d}E/\mathrm{d}x$ and ideally should keep on increasing as the energy of the incident particle also increases, but this rise is canceled due to the density correction term [12].

We mentioned that, to apply the Bethe-Bloch equation, the incident particle has to be a heavy charged particle, and electrons and positrons are light charged particles. This condition exists because the derivation involves assuming that the incident par-

ticle remains undeflected as it traverses through the medium. With electrons, we also arrive at the indistinguishability problem when it collides with other electrons of the medium. But one can still modify the Bethe-Bloch equation to obtain an equation for stopping power [12]. Additionally, Bremsstrahlung also has to be factored in to calculate energy loss through the same process.

2.2 Interaction of Photons With Matter

The interaction of photons with matter happens majorly through the Photoelectric effect, the Compton Effect, and the Pair-Production Effect. Depending on the properties like the incident energy of the photon, the cross-sections of each of these processes vary.

The photoelectric effect refers to the emission of electrons when a photon interacts with it. It occurs when the energy of the incident photon is higher but around the magnitude of the atom's ionization energy. Sometimes the photon can eject an inner shell electron followed by rearrangement of electrons in the atom producing another photon or electron during the process.

The Compton effect occurs when the energy of the incident photon is to some extent more significant than the ionization energy of the atom. It is the process of transferring some of the energy and momentum to an electron the photon collides with. Similar to Compton scattering, we also have Thomson and Rayleigh scattering. Thomson scattering is the scattering of photons by free electrons, but in the classical limit (low energies). Rayleigh scattering is the scattering of photons by atoms acting as an entity.

The Pair-Production effect is observed when the incident photon is of energy greater than twice the mass of an electron. Pair production often refers to a photon creating an electron-positron pair near a nucleus.

As explained, the above processes come into the picture at different energies of the incident particle. In more rigorous terms, the cross-sections of the above processes vary with different energies of the incident particle. Figure 2.1 is an example of the same. Note that coherent scattering is another name given to Thomson scattering and incoherent scattering is Compton scattering.

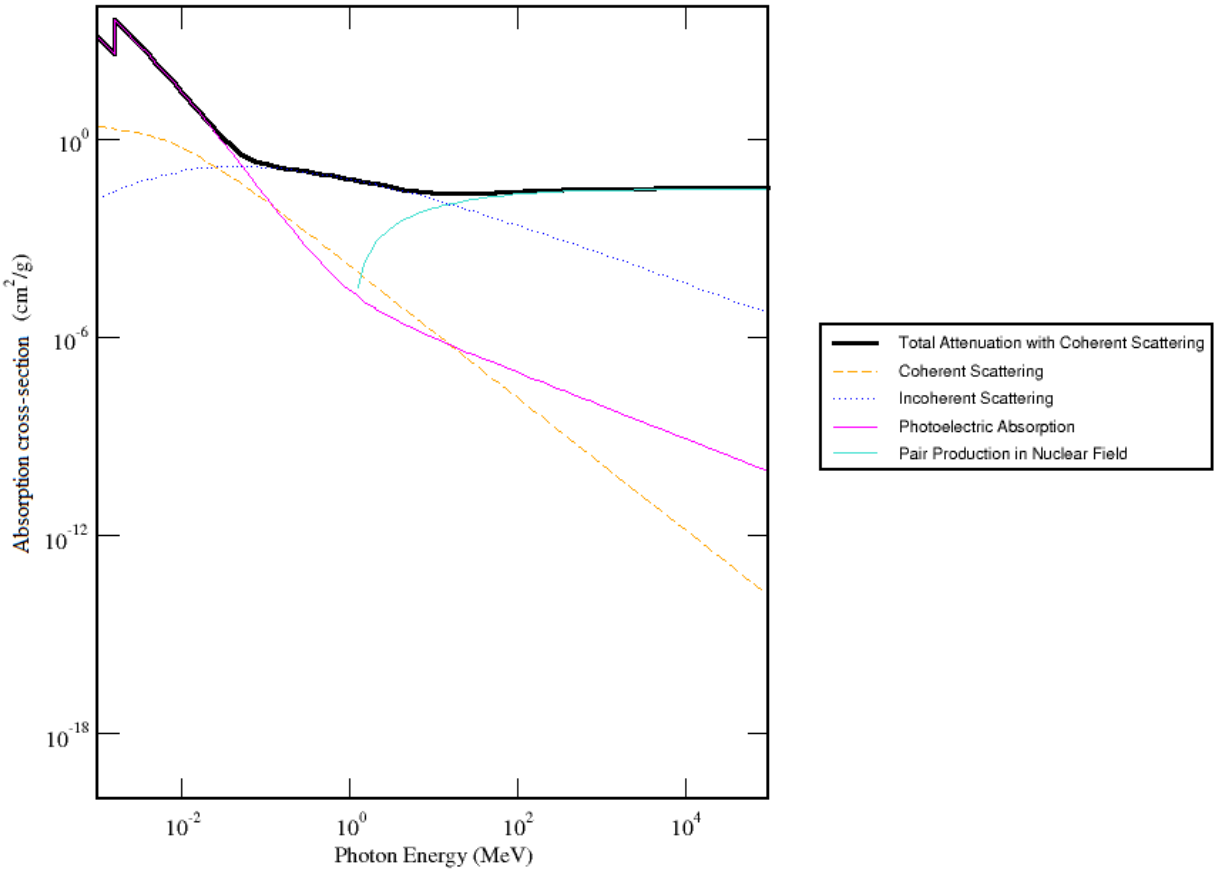

Figure 2.1: Total photon absorption cross-section for Aluminium. Source: National Institute of Standards and Technology.

2.3 Interaction of Neutrons With Matter

Neutrons are particles with no charge and hence are not involved in any electromagnetic interaction with charged particles at the energies we are concerned with. However, they can interact with other nuclei through the following processes [12]:

1. Radioactive neutron capture
2. Fission
3. Elastic and inelastic scattering from nuclei
4. Nuclear reactions where the neutron is absorbed into the nucleus and charged particles are emitted.

Chapter 3

Introduction to Gaseous Detectors

It is quite fascinating how a seemingly-simply process like ionization can lead to a vast range of detector designs, particularly through avalanche processes. The underlying principle in most gaseous detectors in one form or another is electromagnetic interactions. Once an incident ionizing particle enters a gaseous detector, it ionizes and produces one or more primary electrons. External electromagnetic fields present provide kinetic energy to these electrons to accelerate and gain enough energy to create secondary interactions and produce more ion-electron pairs, thus generating a readable output. There are different innovative designs of gaseous detectors to achieve the above characteristics. Before we start describing the evolution of gas detectors since their advent, we will look at features governing the behavior of gas detectors.

3.1 Physical Processes in Gaseous Detectors

3.1.1 Mobility of Charge Carriers

Electrons and ions formed when an ionizing radiation passes through the detector volume gain kinetic energy due to the external electric field present. The velocity of charged carriers depends on the electric field (the average velocity it attains is called the drift velocity) and on the thermal motion. The drift velocity of the ions is given by the following equation:

$$v = \mu \frac{X}{p} \tag{3.1}$$

where v is the drift velocity, μ is called the ion mobility, X is the electric field strength, and p is the pressure of the gas. μ is a factor that depends on the gas used and is inversely proportional to the molecular mass of the gas. Equation 3.1 is valid when (X/p) is small. A typical value of ion mobility for Argon ions is $1.9{\times}10^3$ Torr.cm^2/(V.s). In this limit, the mobility of electrons is around 10^6 Torr.cm^2/(V.s), thus meaning that electrons are about 1000 times faster than ions in the gas volume. When (X/p) is large, the drift velocity is given by:

$$v = \text{const} \times \left(\frac{X}{p}\right)^n \tag{3.2}$$

where n lies between 0.5 to 0.8 [11].

3.1.2 Avalanche Multiplication

Let us say a primary electron is created in the gas medium, and λ is the mean free path of the electron for a secondary ionizing collision, then $\alpha = 1/\lambda$ (also known as the first Townsend coefficient) is the probability of an ionization per unit path length (See Appendix A.2 for more details). This coefficient varies for different gases and for n primary electrons, we have:

$$\mathrm{d}n = n_0 \alpha \mathrm{d}x \implies M = \frac{n}{n_0} = \exp(\alpha x)$$

where M is the multiplication factor, or the gas gain. In the case of non-uniform fields, α is a function of the field, in which case, we have:

$$M = \exp\left(\int_{x_1}^{x_2} \alpha(x)\mathrm{d}x\right) \tag{3.3}$$

The dependence of α on the gas pressure and electric field strength is given by [12]:

$$\frac{\alpha}{p} = A \exp\left(\frac{-Bp}{E}\right) \tag{3.4}$$

where p is the pressure, and A and B are parameters depending on the gas used.

3.2 Modes of Operation

To study the modes of operation of a gas detector, let us consider a proportional counter (made from a cylinder of conducting material (cathode) and a thin wire (anode) inside the cylinder. The cylinder is sealed to make it gas-tight with a window. When an ionizing radiation enters the detector volume, there are primary electrons created through ionization, and the energy that these electrons gain is dependent on the external electric field present.

At zero voltage, there is no current collected as the primary electrons recombine with the ions, but as the voltage is slightly increased, electrons are able to overcome the recombination forces and reach the anode. This is known as the recombination region. As one reaches the ionization chamber region, all the primary electrons created reach the anode. But the curve is flat in this region, which is because even with an increase in voltage, the electrons do not gain sufficient energy to ionize further atoms. Secondary ionizations occur after a certain voltage, and this marks the beginning of the proportional region. For voltages in this region, the secondary electrons created

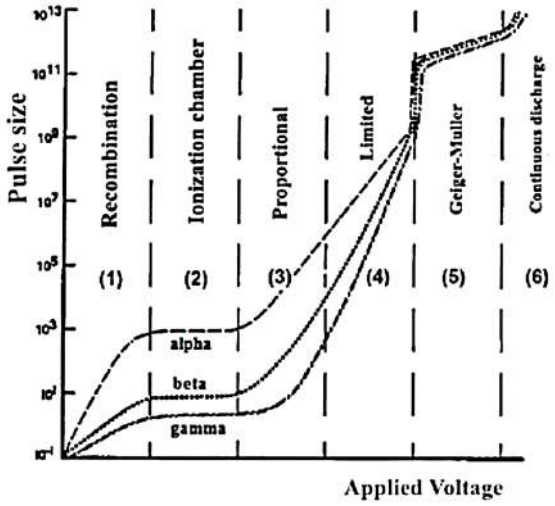

Figure 3.1: Modes of operation of a gas detector. Source: Evolution of Ionizing Radiation Research.

also accelerate to produce more ionization and so on. The number of electron-ion pairs in the avalanche is directly proportional to the number of primary electrons. Beyond the proportional region, the charges created distort the electric field leading to a loss of the proportionality. This region is called the region of limited proportionality. For voltages beyond this region (Geiger-Muller region), the energies gained are so high that discharges are produced, and avalanches spread out along the entire anode wire. The last region is known as the continuous discharge region, where the field in the detector is so high that it itself ionizes the gas and produces discharges.

Today we have access to adequate technologies to detect the signal output when a gas detector is operated in the first four regions. Such technology was not present during the time the first gas detector (the GM counter) was invented. When a detector is operated in the GM region, there are discharges upon being incident with radiation, and these discharges can be seen and heard. The fact that we do not need sensitive equipment to operate this device was what led to the invention of the gas detector. One point to note is that this device was operated at low pressure. The drift velocity of ions and electrons is inversely proportional to pressure (as can be seen in Equation 3.1 or 3.2), leading to higher energies at lower pressures.

Development in technology over time gave rise to the possibility of operating gas detectors at lower voltages. One such detector was the proportional counter, whose structure was briefly introduced and explained at the beginning of this sub-section. In 1968, Georges Charpak invented the Multi-Wire Proportional Counter (MWPC), and this invention set the advent of a plethora of gaseous detectors that followed. We will not go into the details of all the gaseous detectors but instead offer a brief

description of some of the standard gaseous detectors. Sections 3.3, 3.7 and 3.8 will cover the proportional counter, GEM and Thick-GEM detectors in a bit more detail as they pertain to the main topic of this project.

3.3 Proportional Counter

A proportional counter consists of a cylinder that acts as the cathode and an anode wire placed inside the cylinder along the axis of the cylinder. The cylinder is filled with a gas mixture, and there is an entry window for the incident radiation to enter the detector volume.

When a positive voltage is supplied to the anode wire, the electric field inside the detector volume can be calculated using the Laplace equation and the continuity of the electric field. Let us say a and b are the radii of the anode wire and outer cylinder, respectively. Then for a point 'r' distance away from the axis of the wire (a $\leq$ r $\leq$ b), we have:

$$V(r) - V(a) = -\frac{\lambda}{2\pi\epsilon_0} ln\left(\frac{r}{a}\right)$$

where λ is the charge density of the wire, and V(a) is the voltage applied to the anode wire. Using the boundary condition we have (voltage at the surface of the outer cylinder), we get:

$$V(b) - V(a) = -\frac{\lambda}{2\pi\epsilon_0} ln\left(\frac{b}{a}\right) \implies \lambda = -\frac{2\pi\epsilon_0}{ln(\frac{b}{a})}(V(b) - V(a))$$

After using the above two equations, setting V(b) = 0 (we ground the outer cylinder in the proportional counter), and using E(r) = $\frac{\lambda}{2\pi\epsilon_0 r}$, we get:

$$E(r) = \frac{V(a)}{r\,\ln(\frac{b}{a})} \tag{3.5}$$

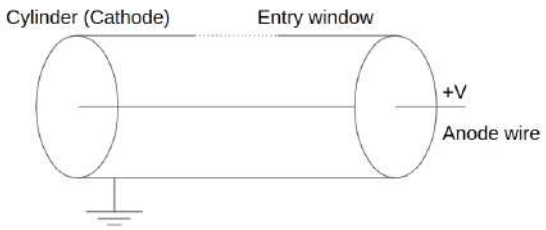

Figure 3.2: Schematic diagram of a proportional counter.

To show how high electric fields are achieved in a proportional counter, let us take an example of a cylinder of radius 1 cm and an anode wire of radius 0.01 cm. If a voltage of 2000 V is supplied to the anode wire, Equation 3.5 tells us that at a distance of 0.011 cm from the center, an electric field of around 40 kV/cm is achieved. Higher electric fields for distances closer to the anode wire.

When an ionizing radiation enters the detector volume, there are electron-ion pairs generated in the gas volume. Due to the electric field, the ions drift towards the cylinder, and the electrons drift towards the anode wire. As electrons drift towards the wire, the magnitude of the electric field increases, and they achieve enough energies to ionize further atoms. This initiates an avalanche effect, thus inducing a readable current in the anode wire. The signal induced consists of a sharp rise and a long tail. There are two factors that give rise to such a signal. The drift velocity of electrons is much higher than that of ions, so the signal induced from electrons rises and falls fast, but since the ions are drifting towards the cylinder slowly, they contribute to a long tail in the signal. Secondly, most of the electrons and ions are formed close to the anode wire, so the electrons travel a short distance to reach the wire as compared to the ions needing to travel almost the length of the radius of the cylinder (which is usually in the order of centimeters).

3.4 Multi-Wire Proportional Counter

The MWPC is what one would obtain if multiple proportional chambers were duplicated and combined. It consists of a set of thin, parallel, and equally spaced anode wires between two cathode planes. Negative potentials are applied to the cathode, and the anode is grounded. Once an incident ionizing particle ionizes the gas molecules as it traverses through the detector, electron-ion pairs are generated, and they start drifting towards the electrode. The electric fields present in this setup are sufficient to provide enough energy to ionize further electrons and thus generate a readable signal. The cross-sectional schematic diagram of the MWPC is shown in Figure 3.3.

The MWPC has a good spatial and energy resolution, but issues persisted with the rate capability, and owing to the slow evacuation of positive ions, a buildup modified the electric fields. Nevertheless, the MWPC gave rise to the advent of detectors based on unique ideas like the drift chamber. Then the drift chamber and the MWPC coalesced to form the Time Projection Chamber.

3.5 Micro-Strip Gaseous Chamber

ok The advances made in photo-lithography techniques and microelectronics helped with the creation of the Micro-Strip Gaseous Chambers (MSGCs), which can achieve

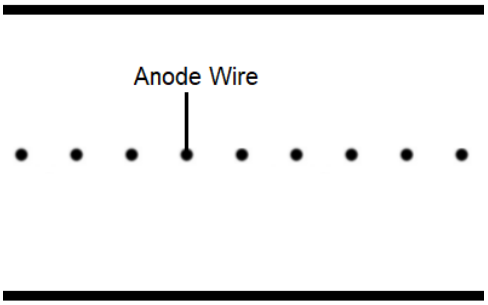

Figure 3.3: A cross-sectional schematic diagram of an MWPC.

rate capabilities of around 10^6 counts $\text{mm}^{-2}\text{s}^{-1}$ when compared to 10^4 counts $\text{mm}^{-2}\text{s}^{-1}$ in MWPCs [9]. The MSGC consists of alternately placed narrow and wide thin metallic strips placed on an insulator. There is also a drift cathode plate on top. The narrow and wide strips are anodes and cathodes, respectively, and the electric fields around these strips can increase to orders of kV/cm. As mentioned in Ref. [9], and [7], the form of the electric field is such that the ions produced by the avalanche evacuate rapidly, thus crossing the hurdle MWPCs could not by providing better rate capabilities.

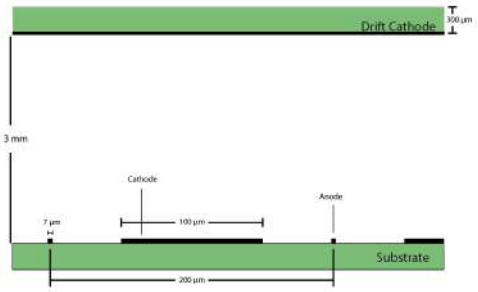

(a)

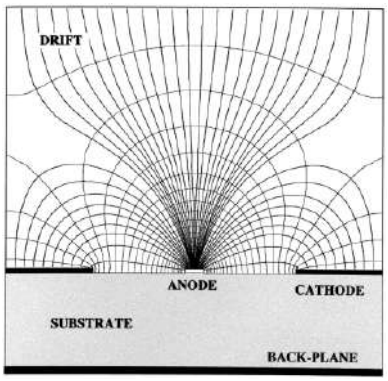

(b)

Figure 3.4: (a) A schematic cross-sectional diagram of the MSGC with typical dimensions. (b) The electric field lines of the MSGC. Source: [17]

One particular disadvantage of MSGCs is charging up effects (in the insulating surface at the bottom). This arises due to the diffusion of electrons and ions generated during the avalanches. The charges accumulated can result in discharges that can melt the metallic strips. In a later section, we will see how the Thick-GEM detector is a more robust detector with respect to these kinds of issues than most gaseous detectors.

3.6 Micro Mesh Gaseous Detector

Until now, we have described detectors with wires or strips; the MICRO MEsh GASeous (micromegas) detector, on the other hand, introduces a mesh in between. In this detector, the gas volume is divided into two by a metallic micro-mesh. However, the multiplication region (the region below the mesh, about 50-100 μm in height) is very narrow compared to the region above the mesh. There is a drift electrode on top and readout strips on the bottom. The amplification happens around and under the mesh. High electric fields (40–80 kV/cm) are created in the amplification gap by applying a voltage between the grid and the anode [7].

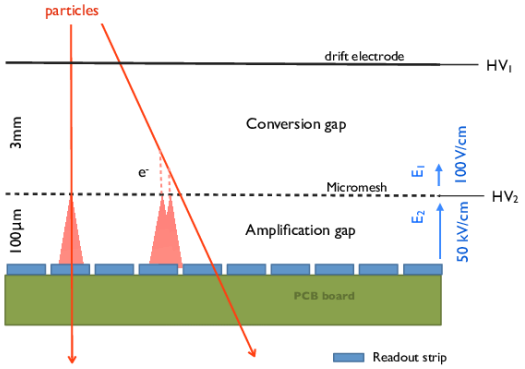

Figure 3.5: Schematic diagram of the micromegas detector. Source: Performances of anode-resistive Micromegas for HL-LHC.

As explained in [9], these detectors offer good spatial resolution and have a fast response owing to the small amplification gap, where the large number of electrons produced have to travel for a small distance to reach the readout.

3.7 Gas Electron Multipliers

In 1996, Fabio Sauli introduced GEMs [16], which are electron multipliers made from a copper-cladded polymer foil perforated by a high density of holes. The GEM electrode is pierced by a regular array of hourglass-shaped holes and is produced by certain etching techniques. High voltages are applied on both copper surfaces to provide for a high voltage gradient. The hole shape of the foil is such that there is a dipole-like field (See Figure 3.6b) that can help with a focused electron path at the center and high gains through multiplication because of the high field values in the hole.

The GEM detector is similar in design to the previous detectors. There is a drift electrode above and readout strips underneath the GEM foil, respectively. The typical dimensions and specifications of the detector will be discussed soon.

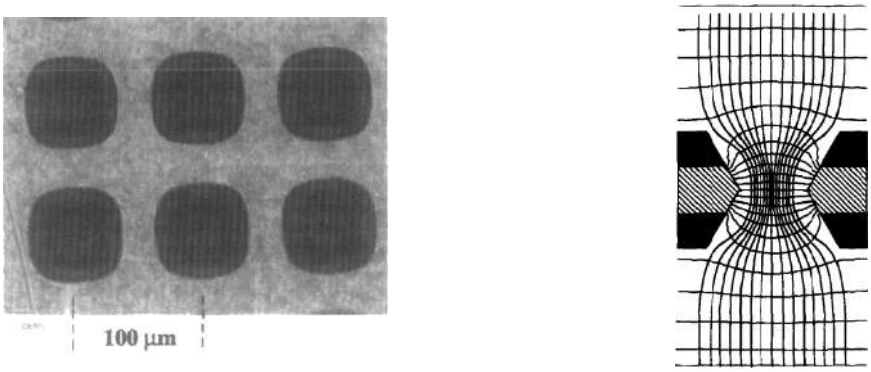

(a) (b)

Figure 3.6: (a) A top view image of the GEM foil. (b) The electric field lines across a GEM hole. Source: [16]

When an ionizing particle passes through, it produces primary charges by ionization. Through drift and diffusion processes, the charges are transported through the gas volume to the amplification region close to the electrodes. These charges will attain high velocities due to the high electric field and cause further ionizations leading to an avalanche effect. This avalanche process is also called the Townsend avalanche and is studied in great detail in Ref. [17]. The first Townsend coefficient is a variable that has been extensively studied in gaseous detector physics and represents the number of ion pairs produced per unit length of drift [17]. These charges are then collected by the readout pads under the GEM electrode. Separated from the multiplying electrode, the charge collection and readout plane can be patterned at will with strips or pads; usually, they are a set of perpendicular strips to serve as a 2-dimensional readout.

As explained in [17], the GEM detector, with cascaded GEM foils, can reach very high gains without getting destroyed. This is a crucial point because previous detectors like the MSGC involved damages when attempts to reach higher gains were made. The readout also can be patterned depending on the user's needs.

3.8 Thick-Gaseous Electron Multipliers

The Thick-GEM detector is a variant of the GEM detector with dimensions blown up by some factors (details of which we will get to soon), but some structural aspects are different. Thick-GEMs have a cylindrical hole shape compared to an hourglass

shape in GEMs, which also means the etching process to make these holes is different. Keeping in mind the difficulty in making a precision device such as a GEM foil with its very fine hole diameter along with its small pitch, the Thick-GEM came out to be a device cheaper and easier to manufacture. Furthermore, Thick-GEM detector is also very "robust", which means that it has good strength against mechanical force, high electrical fields, ease of handling, etc. As mentioned before, other detectors like the MSGC can get destroyed while operating at high fields; typical GEM electrodes are also sensitive to sparking and can be permanently damaged after a significant discharge. However, the etched rim in a Thick-GEM helps reduce edge discharges [5]. To make a GEM electrode, one needs high-precision tools to make structures at such dimensions, but the Thick-GEM can be made without such stringent requirements. Figure 3.7 and Table 3.1 gives us a better idea of the difference between both detectors in terms of foil specifications.

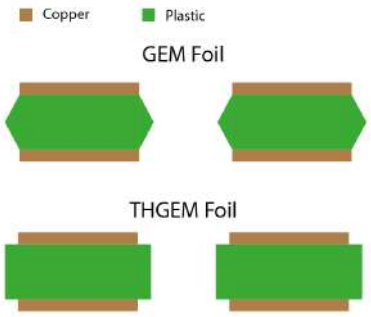

Figure 3.7: Cross-section schematic of the GEM and Thick-GEM holes (Not to scale).

Measurement	GEM	Thick-GEM
Hole Diameter (Inner)	50μm	0.4mm
Hole Diameter (Outer)	70μm	0.6mm
Pitch	150μm	1mm
Thickness	60μm	0.5mm
Electric Field	30-80kV/cm	15-25kV/cm

Table 3.1: Comparison of some specifications between a typical GEM and Thick-GEM foil.

Chapter 4

Development of the Thick-GEM Detector

4.1 Overview

This Chapter will deal with the intricate details of the work done to fabricate and assemble the Thick-GEM detector and discuss the results obtained from a few simulations that were performed using Garfield++ [1]. The main paper that was referred to for guidance is Ref. [21]. It is to be noted here that the fabrication process was a continuation of the work done by me during a previous project. In particular, everything described after Sections 4.2 and 4.3 in this Chapter was done as part of the Master's Thesis.

The detector comprises three main elements: the drift electrode, the Thick-GEM foil, and the readout pads; all of them are placed inside a gas enclosure, with a window on top that is transparent to incoming particles but yet keeps the detector air-tight. The drift electrode is usually a metallic mesh with a voltage to provide a drift field, usually of magnitude 2kV/cm. As the name explains, the drift electrode makes the charges produced under it attain a drift velocity, so they are directed towards the Thick-GEM electrode. The electric field produced in the Thick-GEM holes due to the voltage supplied on both copper surfaces is usually around 30kV/cm. Under the Thick- GEM electrode is the induction gap with an electric field, usually around 1kV/cm. This region helps in directing the electrons to the readout pads where the signal-current is generated, thus giving us a readable output. The entire setup will be in an airtight gas enclosure made with perspex on the sides, Mylar as the top layer (also serving as a window for incoming particles), and the bottom will be a PCB board with readout pads. The detector can be divided into three regions based on the electric field values that will be applied, namely the drift region, Thick-GEM hole region, and the induction region. The same has been labeled in the schematic diagram shown in Figure 4.1. The Thick-GEM foil we are using is 0.25 mm thick, and inner and outer hole diameters of 0.2 mm and 0.3 mm, respectively. The pitch between the holes is 0.45 mm. The following components are needed to construct the detector fully:

- Outer air-tight enclosure and top-enclosure

- Readout strips
- Drift electrode
- Electronics

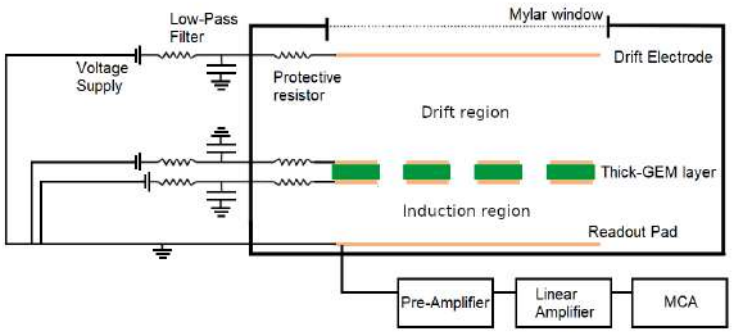

Figure 4.1: A cross-sectional schematic diagram of the detector and the electronic circuits used.

The subsequent sections will describe the components and provide details of the manufacturing process, if relevant.

The drift electrode is essentially Aluminum tape pasted on a Mylar sheet (with a contact for a connection to the voltage source). The sheet is held by a Poly-Lactic Acid (PLA) frame (3D printed) to provide support and keep it flat so it does not bend due to its weight. The dimensions of the working area of the drift electrode is 10×10 cm^2. Under the drift electrode, is the Thick-GEM foil which has three layers, a top copper electrode, a middle FR4 layer, and a bottom copper electrode. The total working area of the Thick-GEM foil is also 10×10 cm^2. The anode then comes under the Thick-GEM foil, which in our case are the readout strips. The Thick-GEM foil and the drift electrode are kept at a height of 2.5 mm and 7.5 mm from the base respectively using nuts. There is thus a gap of 5 mm between the drift electrode and the Thick-GEM foil. Figure 4.1 is a schematic diagram explaining the same.

There are rectangular copper strips provided at the drift electrode and Thick-GEM foil for the voltage connection (See Figure 4.2). The contacts from different layers of the electrode have been connected to other contacts for extension purposes, which will come out of the gas enclosure and can be understood by looking at Figure 4.3. This makes applying the required voltages to each layer outside the air-tight enclosure easier.

We finally close everything with an enclosure of height 1.5 cm, which will make the entire setup airtight, and we also provide an inlet and an outlet valve for gas flow (See Figure 4.4). The top portion of the enclosure is made of PLA and a Mylar

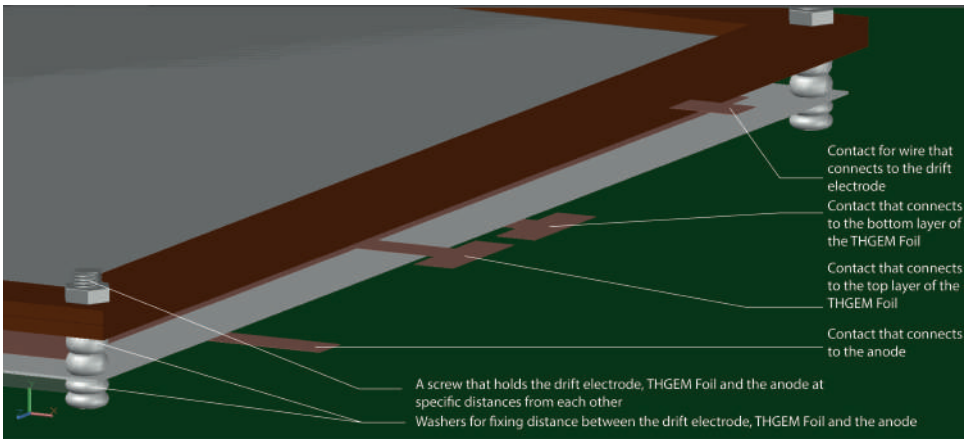

Figure 4.2: Isometric view of the design of the detector made using AutoCAD.

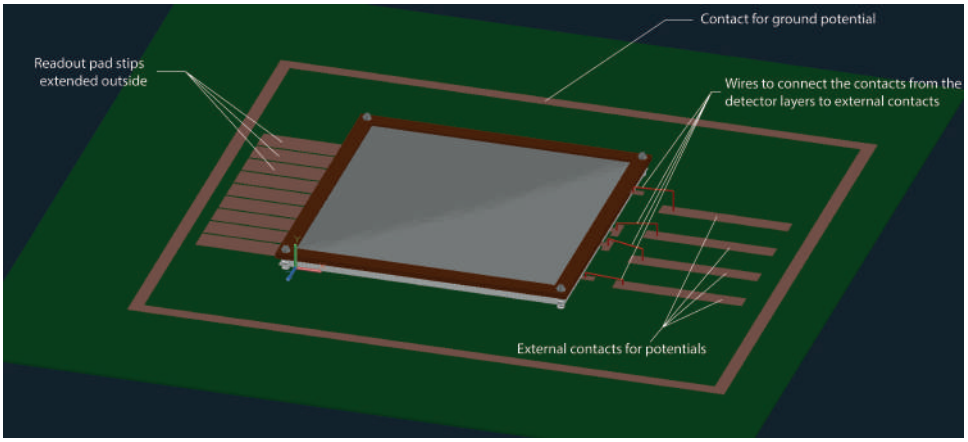

Figure 4.3: Second isometric view of the detector.

window (which would serve as a window for incoming particles). Perspex is used for the sidewalls of the air enclosure.

The contacts for the four potentials for the detector will all be connected to a serial 10 MΩ resistor, a 50 Hz low pass filter (using a 2.2 nF capacitor and a 10 MΩ resistor), and then to the power supply, which is a CAEN N1470 High Voltage (HV) supply. The series resistance is added as a protective resistor (against current surges), and the low pass filter is to limit AC voltages that can arise from the voltage supply. We will see that frequencies in voltages can act as a source of noise in a later section. The potentials that will be supplied to the contacts are as shown in Table 4.2.

For the potential values applied, the electric field magnitudes for different regions would correspond to the values shown in Table 4.2. These were also the same field values used in Ref. [21]. But there are no universally fixed field values for these re-

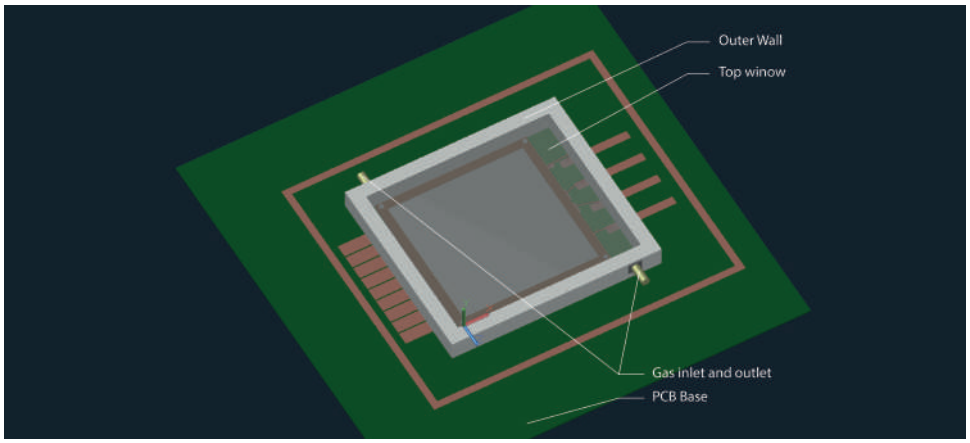

Figure 4.4: Top view of the detector showing the two electrodes and the Thick-GEM Foil.

Surface	Potential (V)
Drift Electrode	-2000
Top layer of Thick-GEM foil	-1500
Bottom layer of Thick-GEM foil	-1000
Anode	Gnd

Table 4.1: Typical potentials that are supplied to each electrode in the detector.

gions. They vary based on the detector specifications and other aspects like materials used, quality of assembly, etc.

Region	Height (mm)	Field (kV/cm)
Drift region	5	1
Thick-GEM hole region	0.25	20
Induction region	2.5	2

Table 4.2: Dimensions and electric field magnitudes for different regions in the detector

The readout strips were connected to the preamplifier, a linear amplifier (CAEN Spectroscopy Amplifier M968), and a Multi-Channel Analyser (MCA) (Ortec 927 ASPEC MCA), and finally, a computer to store the output from the MCA.

4.2 PCB and Readout Strips

Ten readout strips made of conducting material (Copper in our case) were required to be placed under the Thick-GEM electrode. So a Printed Circuit Board (PCB)

board with copper-clad on both sides was taken as the base from which Copper will be etched out, leaving only the readout strips behind.

In order to etch out the unwanted copper, we carried out a displacement reaction using a $FeCl_3$ solution. The corresponding displacement reaction is as follows:

$$FeCl_3 + Cu \rightarrow FeCl_2 + CuCl$$

We prepared a mask using readily available toner ink, which acted as a physical barrier, under whose region the $FeCl_3$ would not react. So after dipping the board in this solution $FeCl_3$ would remove copper wherever the mask was not present. Using a laserjet printer, we printed the mask layout on OHP sheets (these are transparent sheets used for Over-Head Printers, from where the name arises). These sheets were then placed at appropriate positions on the PCB board and ironed, due to which the toner ink on the sheets was transferred to the PCB board, thus completing the masking process. Then an appropriate $FeCl_3$ solution was prepared, and the board was placed in the solution and was agitated until all the copper from the desired regions was removed. We washed the toner ink with Propanol to remove the mask, which removed the ink but not the Copper under it. An image of the board after this etching process is shown in Figure 4.5.

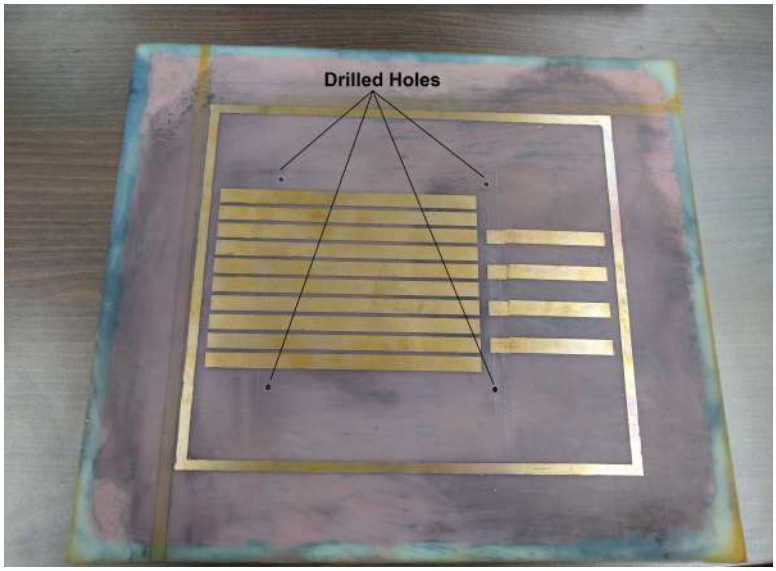

Figure 4.5: The PCB with the readout strips and other terminals after the chemical etching process. Four holes were also drilled, which will be used to hold the Thick-GEM foil and the drift electrode.

4.3 Drift Electrode

The drift electrode was made with Aluminum, Mylar, and a frame to hold the Mylar and Aluminum flat and sturdily. The support structure frame is made of PLA and was designed and 3D printed (printed using NISER's Robotics Club's 3D printer). Then a Mylar sheet was stuck on top of the frame to serve as a base for the Aluminum tape to be pasted upon. The voltage supply would be connected to this Aluminum layer with the voltage as mentioned in Table 4.1.

(a) (b)

Figure 4.6: (a) The Perspex frame with the inlet and outlet valves. (b) The rubber layer that will be placed on top of the Perspex layer to act as a seal for the joint.

4.4 Gas-Tight Enclosure

The Thick-GEM detector has an inlet and an outlet for gas flow, and the remaining volume needs to be airtight. To form a gas-tight container around the anode, foil, and drift electrode, we made four walls using Perspex along with an inlet, and an outlet for the gas flow (See Figure 4.7a), with a top enclosure. The interior dimensions were approximately 15.4×14.4×1.5 cm^3. The top enclosure was made with a 3D printed structure with an open window that was covered with Mylar which would serve as an entry for incident radiation.[1] The objective was to make a top enclosure that can be opened and sealed if we needed to change components or perform some checks. All components inside this chamber would be in an gas tight environment, with gas being brought in and flushed out at a constant rate.

Since the side walls were sealed with Araldite, they are never tampered with and do not account for any gas leak. The Mylar sheet that would be placed for the window

[1] Although can be included in a future test, we do not know if PLA would allow particles of our source (5.9 keV X-Rays from ^{55}Fe) to pass through, whereas Mylar and Kapton are materials used as a window for irradiated particles to pass through [6].

was pasted and sealed with Araldite. The only source for a gas leak can arise from the top enclosure, and motivated by the design of O-ring joints [13] (See Figure 4.8a) that are used in vacuum chambers, we designed an enclosure that, when tightened to the Perspex frame with screws, can form an air-tight joint. We experimented with many designs, but the final top enclosure has a protruding ridge from the flat surface (See Figures 4.7c, 4.8c). The entire wall was drilled with holes so that screws can go all the way and be able to lock the top enclosure to the Perspex walls. For a good seal, we cut a rubber mat and placed it on top of the Perspex later (See Figure 4.7b). Gas leak tests were also conducted with different materials like thermoplastic elastomers[2], foam, Teflon layers, etc.

(a) (b) (c)

Figure 4.7: (a) The Perspex frame with the inlet and outlet valves. (b) The rubber layer that will be placed on top of the Perspex layer to act as a seal for the joint. (c) A zoomed-in image of the top enclosure to show the ridge.

We performed a gas leak test, i.e., measured the rate at which gas leaks for different pressures for the design that was finalized. We flow some gas inside the detector and then block the inlet and outlet valves, leaving the detector with gas inside it at some initial pressure. We then note the pressure inside it (using a U-tube manometer) at certain intervals of time. The initial designs had performed very badly, losing all air in a matter of seconds. The manometer does not provide us with information about where the leak is occurring. We then gauged the amount of gas leaking and regions from where it is leaking by placing the setup (without the foil, drift electrode, and electronics, but with the gas flow) underwater. This gave rise to bubbles from locations where the setup has gaps or holes. When we arrived at a setup where there were no bubbles visible, the pressure drop (measured with the manometer) was still not satisfactory. Dipping the setup in soap water instead of water further provided us with additional areas of improvement that were needed to make the setup leak-proof. After these changes, the plot of pressure inside the container vs. time was plotted and is shown in Figure 4.9b, but after tightening the screws of the joint between

[2]a material that increases in tack when heat is applied; such materials used in glue-guns

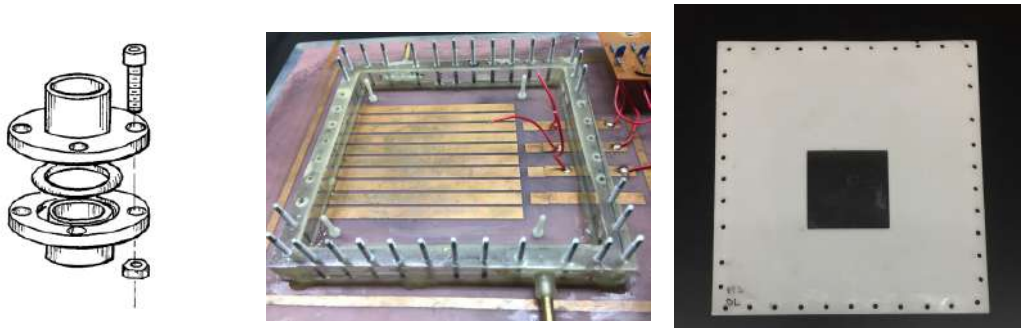

(a) (b) (c)

Figure 4.8: (a) An O-ring sealed vacuum connection (Source: [13]). (b) An image of the detector after the placement of the Perspex walls and installation of screws taped with Teflon to prevent gas leaks. (c) Image of the top enclosure.

the Perspex frame and top enclosure, the subsequent gas leak test (See Figure 4.9b) which was performed for a larger period) gave a lesser leak rate.

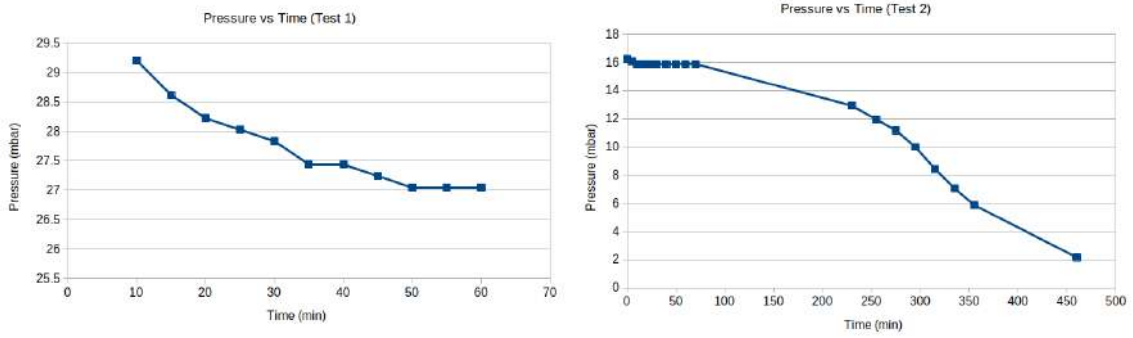

(a) (b)

Figure 4.9: Gas leak rate for the (a) first attempt and (b) second attempt (tighter joint).

Based on a couple of gas-leak tests, we were able to obtain an average leak rate of about 2.2 mbar/hour. For comparison, a recent presentation by a group from Punjab University that assembled and sent GEM detectors to be used in the CMS experiment, showed gas leak rates of (0.4-4.2) mbar/hour. Since the leak rate of the detector we built falls well inside this range, we thus have successfully fabricated an enclosure with an acceptable gas leak rate.

4.5 Assembly in a Clean Room

The hole size of the Thick-GEM foil prevents us from leaving it open to the air, it rather requires to be handled in a clean room so that no dust particles interfere. If any dust particles are present in the detector, then the efficiency of the detector can drop, sometimes even leading to electrical discharges at such high voltages. Before placing the Thick-GEM foil, the detector was cleaned and handled in a class-100[3] clean room at NISER. Furthermore, the Thick-GEM foils were opened and placed inside the cleaned setup, inside a laminar airflow table, which, as the name suggests, has a laminar airflow inside the chamber.

After the Thick-GEM foil was placed, the drift electrode was placed above it, the required HV supply connections were soldered, and the whole setup was closed with the top enclosure, thus making the setup airtight. The design of the detector is such that the HV supply can be made outside without having to open the setup every time we have to change the supply points.

An Ar+CO_2 (70%-30% ratio respectively) was used as the gas mixture, and the setup was flushed with this gas mixture for a few days until the detector was tested.

4.6 Gas Selection and Quenching Gases

The Thick-GEM detector is a gaseous detector, but we never discussed what gasses to use or why use them. For the selection of the gas, one needs to keep in mind that the gaseous constituents should not have a high electron affinity to attract the electron before it even begins the avalanche effect. Keeping in mind the physical conditions required to keep the substance in its gaseous state, noble gases are good choices. After ejecting an electron, one might argue that the noble gas atom attains halogen configuration, but by the time it pulls the electron, the electron under the external electric field would have begun subsequent collisions. There are other favorable reasons for noble gases. Nobles gases are inert, and that is also why they are a good choice, and what is meant by this is that they are chemically inert, so they do not react with the detector materials. They also do not catch fire easily, and this is relevant because sparking is something very likely to happen in such detectors. We do not need gases that catch fire inside during the experiment.

We also add other relatively inert gases like CO_2 and CH_4 to the gas, and they are called quenching gas. This is done to reduce the gain, as a very high gain can also lead to a higher discharge probability. Higher discharge probability means higher chances for the Thick-GEM foil to get destroyed. These gases are electronegative, so at times

[3]To offer some perspective, a class 100 cleanroom contains a maximum of 832 particles greater than a size of 1μm.

they absorb the electron from an ionized atom preventing further amplification.

4.7 Electronics Used

The protective circuits for the HV supply were mentioned before. Additionally, we have the equipment to obtain, shape, and amplify the signal from the readout strips. This section describes the various components and the subsequent electronic circuits/connections. The train of electronics from the readout strips is the preamplifier, amplifier, and MCA.

4.7.1 Preamplifier

The readout strips are first connected to the preamplifier, and we used an Ortec 142 IH charge-sensitive preamplifier (or preamp) [15]. The primary function of a preamplifier is to extract the signal (which in our case, are charges that originate due to primary and secondary ionizations) without degrading the signal-to-noise ratio. This is usually why the preamplifier is placed close to the detector, so that the characteristics of the signal are not disrupted by factors like capacitance changes by cabling, radio-frequency pickup, etc. A charge-sensitive preamplifier is generally used for energy spectroscopy, and these preamplifiers can measure the quantity of charge and time of arrival. A preamplifier would consist of an operational amplifier with a feedback capacitor, which acts as a charge integration circuit, thus converting the number of charges to a voltage value. The amplitude of the output is proportional to the quantity of charge.

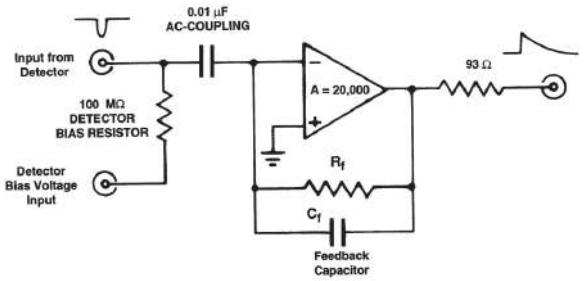

Figure 4.10: A circuit diagram of a typical charge-sensitive preamplifier. This figure shows how a typical input pulse and output look like. Source: [15]

4.7.2 Spectroscopic Amplifier

The CAEN N968 Spectroscopy Amplifier [20] that was used in the experiment has a variety of functions like amplification, shaping, pile-up rejection, pole-zero cancella-

tion, and baseline restoration. The output of the preamplifier will be connected to the spectroscopy amplifier for further pulse processing.

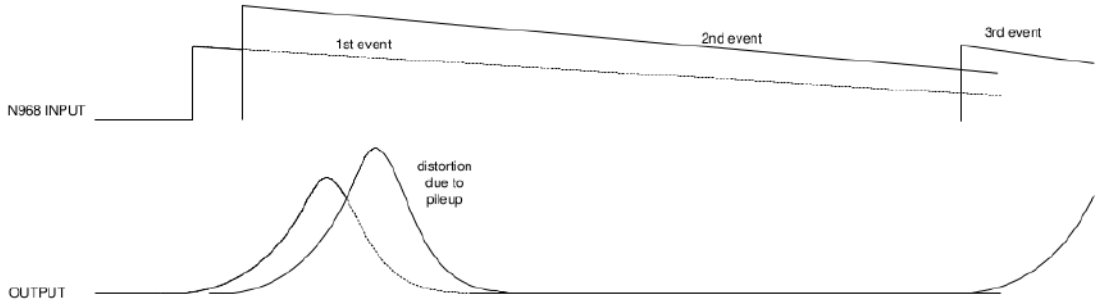

Figure 4.11: A schematic diagram of the input pulse to the amplifier and the output pulse. The inter. We see that the output pulse has been shaped, which is done through a shaping circuit. Source: [20]

The shaping is done through a CR-RC-shaping circuit, and for pedagogical reasons, we describe a simple CR-RC-shaping circuit.

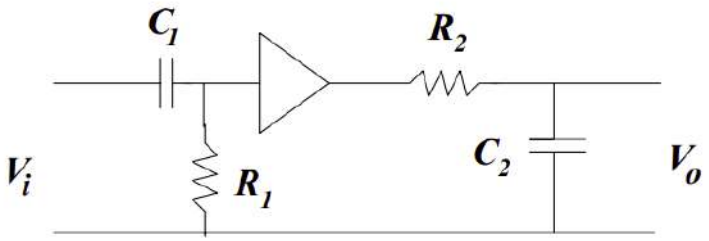

Figure 4.12: The schematic diagram of a typical shaping circuit. Source: [4]

The output of the shaping circuit looks like the output of the amplifier, as shown in Figure 4.11. Additional shaping can be done by varying the time constants of the RC/CR circuits. Figure 4.13 conveys the same.

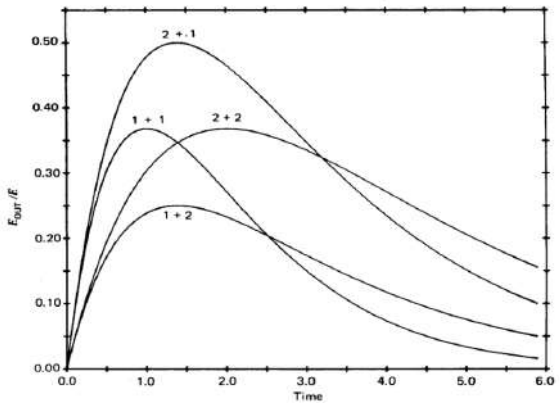

Figure 4.13: The outputs of a CR-RC shaping circuit to a step voltage. Curves are shown for several different combinations of time constants and are labeled as (time constant of CR circuit + time constant of RC circuit). Source: [4]

4.7.3 Multi-Channel Analyser

The MCA is the final piece of equipment we use to process the signal before the information is sent to a computer. The MCA is a device that takes in the shaped and amplified pulse from the amplifier and digitizes it, which means it converts analog information to digital information. We used an Ortec 927 ASPEC MCA for the experiment.

4.8 Preliminary Tests

Before we place a source and start performing any experiments, we need to test for any electrical discharges while increasing the voltage supply slowly. The CAEN HV supply has an inbuilt device to measure the current flowing through the circuit, and the least count can go up to 0.05 μA. To prevent the foil from getting damaged by sparks, we set a limit of 20 μA on the CAEN HV module, and if a current greater than this value flows (which can arise if there are electrical discharges), the supply automatically switches off. These tests were carried out in two stages:

1. We first increase only the voltages on the Thick-GEM layers in steps of 20 V until we reach -1500 V and -1000 V for the upper and lower layer of the Thick-GEM foil, respectively. We observed no current greater than 0.30 μA.

2. We then increase the voltages on the Thick-GEM layers and the drift electrode until we reach -2000 V, -1500 V, and -1000 V for the drift, upper Thick-GEM

layer, and lower Thick-GEM layer, respectively. We observed no current greater than 0.30 μA.

4.9 Measuring the Energy Spectrum of ^{55}Fe Source

Once the required components and circuits that are needed to start taking data are in place (See Figure 4.1 for a schematic diagram of the components needed), we placed a ^{55}Fe source [4] that produces X-Rays of energy 5.9 keV, to which we observed no spectrum. We also got no desired output for a Strontium β source, thus eliminating concerns regarding the activity of the ^{55}Fe source that was used.

A secondary setup we often used is to connect the detector output to the preamplifier and the output of the preamplifier to an oscilloscope (Teledyne Wavesurfer 510) to see if we get an output close to the expected form (a typical output of a signal from the preamplifier contains a very short rise time and a long decay tail, as shown in Figure 4.10). This setup was used for the rest of the experiments mentioned in this Chapter, unless mentioned otherwise.

4.10 Components Check

Given that there are no issues from the leak-proof setup and the source, we performed ablative tests with the help of a pulse generator from Agilent (81110A) to see if any of the electronic components we were using was faulty:

1. The oscilloscope was not found to be faulty after the same square wave pulse that was generated from the pulse generator was seen on the oscilloscope too.

2. The preamplifier has an additional connection called the test input, where one can provide a test pulse for calibration, and this connection can also be used for testing/additional calculations. But according to [15], the test pulse that goes into the test input connection should have a rise time of around 20-40ns and a decay time of 200-400 μs. The same was achieved using an RC-shaping circuit and appropriate characteristics of a square wave from the test pulse generator. The results of this test indicated that the preamplifier has no faults. See Figures 4.14, 4.15 and 4.15.

3. With the same circuit and settings as above, we connected the oscilloscope to the spectroscopy amplifier, which was connected to the preamplifier. The

[4] The ^{55}Fe source produces X-Rays of energy 5.9 keV. This characteristic X-Ray arises because ^{55}Fe converts to ^{55}Mn through electron capture, which in turn leads to a re-arrangement of electrons giving rise through these X-Rays.

output on the oscilloscope from the amplifier was Gaussian-like which implies that the spectroscopy amplifier too is working as expected.

Figure 4.14: The square pulse generated by the pulse generator.

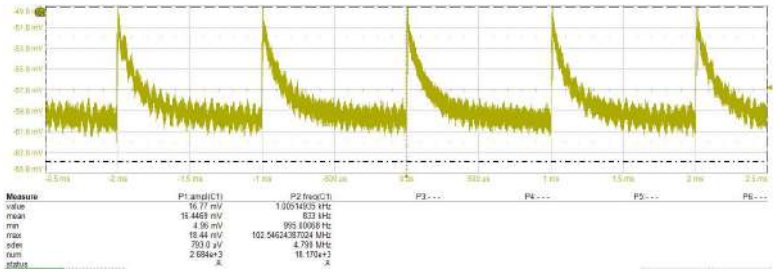

Figure 4.15: The square pulse after being shaped by the RC-shaping circuit.

Figure 4.16: The preamplifier output for the the input pulse shown in Figure 4.15.

Now that the electronic components were found to have no faults, we cornered the problem to the detector or noise [5], or both. The pursuit from here is to reduce noise levels or increase the effective gain of the detector.

[5]Noise can be a reason for not observing the expected output from the preamplifier because there is a possibility that the amplitude of the signal is lesser than that of noise

4.11 Study on the Expected Output

With a rough calculation, we can find out the expected output of the signals when measured from the preamplifier. Doing this exercise would give us an idea of how much noise we should reduce or by what factor the signal should be amplified.

We connected the pulse generator to the test input of the preamplifier and observed the output of the preamplifier on an oscilloscope. For a square wave pulse of height 50 mV, width 60μs, and frequency 500 μs, a preamplifier output with pulses of around the same amplitude was obtained. The feedback capacitor in the preamplifier is what governs the height of the output pulse, and the voltage is given by Q/C_f, where C_f is the capacitance of the feedback capacitor. So we have the following:

$$50 \text{ mV} = \frac{Q}{1 \text{ pF}} \implies Q = 50 \text{ fC}$$

This means that an input charge pulse of 50 fC to the preamplifier would give us an output of height 50 mV.

We now try and calculate the number of expected charges from the detector after amplification for Argon-CO_2 (70%-30%) mixture and 30 kV/cm field in the Thick-GEM hole region. For the ^{55}Fe source that produces X-Rays of energy 5.9 keV, and the mean ionisation energy values (W) for Argon and CO_2 are 25 eV and 34 eV respectively The average number of primary electrons produced by an X-Ray is $5.9 \text{ keV} \times \left(\frac{\%(\text{Ar})}{\text{W(Ar)}} + \frac{\%(\text{CO2})}{\text{W}(CO_2)}\right) = 207.7$ [2]. A more rigorous calculation can be found in Ref. [7].

For a field of 30kV/cm in the Thick-GEM hole region in Ar-CO_2 (70%-30%) mixture, Figure 4.17 gives us a gain of around 200 (but only if the foil was 1 cm thick). But assuming the Townsend coefficient varies linearly for different thicknesses, we expect a gain of the order of 10. Although the value might be approximate for that field, we can always vary the supplied voltage by around 1-2kV/cm to achieve a similar value.

Thus, we predict a maximum of about 2200 primary electrons generated from one X-Ray, i.e., in one pulse. This corresponds to 0.3 fC of charge reaching the readout strips ($\sim$6250 electrons correspond to 1 fC), or 0.3 mV output from the preamplifier.

4.11.1 Simulation of Expected Gain

The results obtained using Figure 4.17 are for Argon-CO_2 (70%-30%) and (90%-10%) mixtures, whereas we have (70%-30%) and (80%-20%) mixtures available. To check the expected gain for an (80%-20%) mixture, we performed simulations for three different fields on Garfield++ using the nearly exact Boundary Element Method

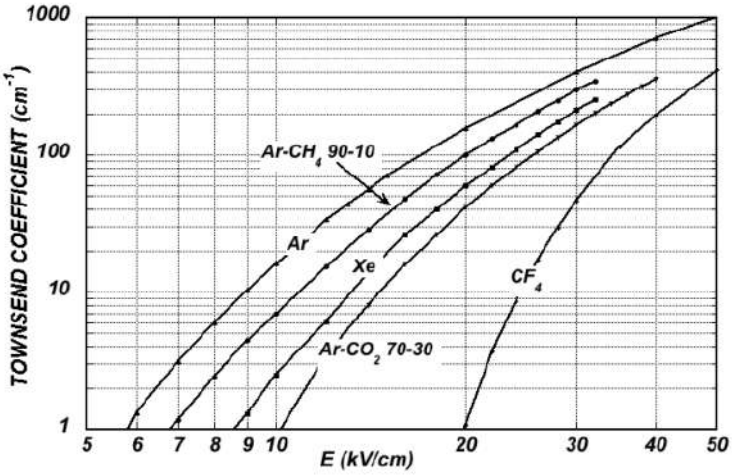

Figure 4.17: Computed first Townsend coefficient as a function of the electric field in several gases at NTP. Source [23]

(neBEM) [14].

Garfield++ is a C++-based toolkit for the detailed simulation of particle detectors that use a gas mixture or a semiconductor material as the detector volume. Garfield++ needs electric field information (the electric field information can be imported to Garfield++ using Elmer [10], COMSOL [8], the neBEM package, etc.), transport properties of electrons in gas mixtures (calculated using Magboltz [3]), and the ionizations produced by relativistic charged particles (can simulated using HEED [19], SRIM [22], etc.). Several other classes help with simulating the initialization of particle tracks, avalanche and drift of the produced primary and secondary particles, and signal calculation.

The neBEM solver uses closed-form expressions of the potential and the field obtained from the symbolic integration of the Green's function of a uniform charge density distributed over a triangular or rectangular boundary element. neBEM first breaks up the system of interest into right triangles and rectangles (they are referred to as primitives), and then the contribution from a primitive (assuming charge is uniformly distributed) is calculated using closed-form expressions (analytical solutions) of the potential and the field obtained from the symbolic integration of the Green's function.

For the detector setup we have used, a unit cell was made, and an image of the same is shown in Figure 4.18.

The voltage biases supplied are as shown in Table 4.3.

The corresponding plots of equi-potential lines are as shown in Figures 4.19a and 4.19b.

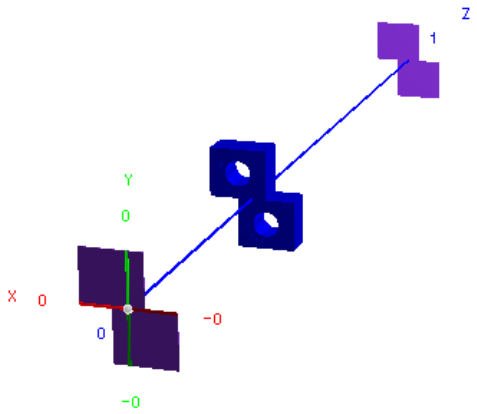

Figure 4.18: An image of the unit cell of the Thick-GEM setup.

Entity	Voltage applied
Drift electrode	-2500 V
GEM top layer	-1500 V
GEM bottom layer	-500 V
Anode	0 V

Table 4.3: Voltages applied to the electrodes.

The equi-potential lines appear to be distorted with something definitely going wrong. A report of this issue was sent to Heinrich Schindler and Prof. Supratik Mukhopadhyay, one of the authors of Garfield++ and neBEM respectively. The setup currently in use has a Thick-GEM foil of pitch 450 μm, and neBEM has only a limited number of solid structures for which electric fields can be calculated. The closest unit cell to that of the required detector with which we can obtain the expected plot of equi-potential lines can be done with a pitch value of 600 μm [6]. The unit cell of this setup is as shown in Figure 4.20a and the plot of equi-potential lines that was obtained is as seen in Figure 4.20b. This unit cell is a solid cuboid with a lesser number of edges as compared to the former unit cell and can be one of the possible reasons as to why this unit cell works and not the previous one.

We then simulated the gain for 1000 events where one event corresponds to an

[6] we also need to note that since we will simulate gain, the new configuration is acceptable as the gain does not vary with pitch [18].

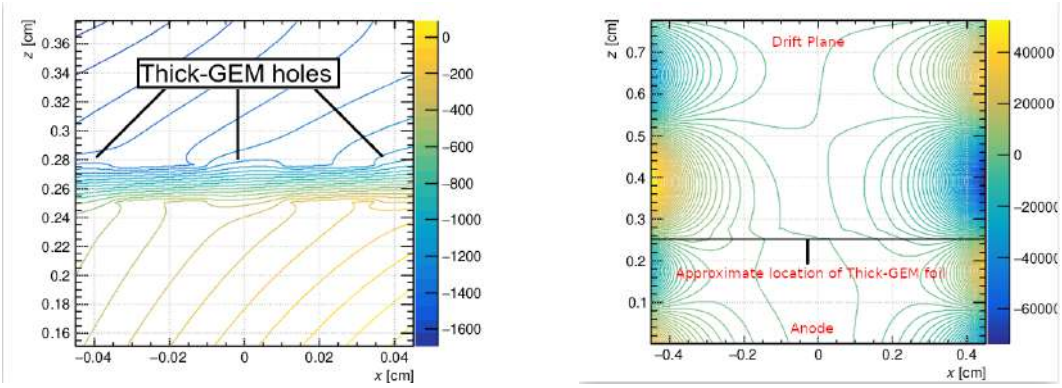

(a) (b)

Figure 4.19: Plot of equi-potential lines (a) across the Thick-GEM foil (across three holes) and (b) across the full detector. The legend on the right for both images are potential values (in V). This was for 20 copies of the unit cell along X and Y directions each.

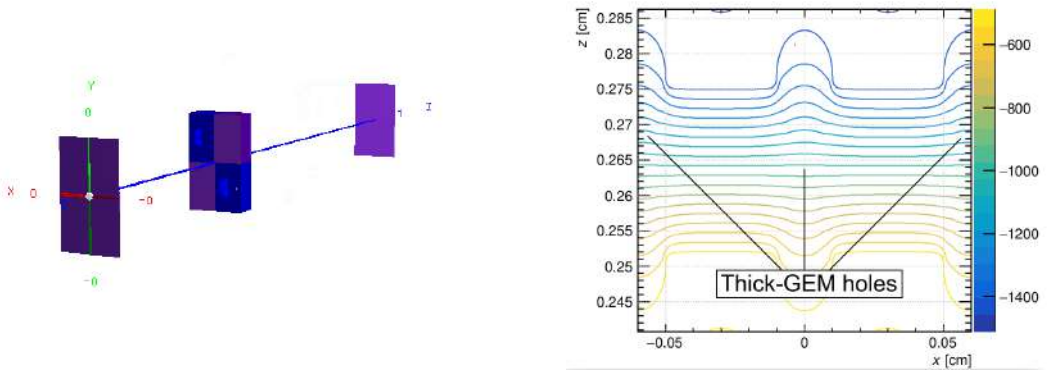

(a) (b)

Figure 4.20: (a) An image of the unit cell of the Thick-GEM setup with new pitch. (b) Plot of equi-potential lines across the Thick-GEM foil (across three holes). The legend on the right for both images are potential values (in V). This was for 20 copies of the unit cell along X and Y directions each.

electron left in the drift region (0.1 cm above the Thick-GEM foil). This was done for 2 kV/cm in the drift and induction region, and three different fields across the Thick-GEM foil (25 kV/cm, 30 kV/cm, and 35 kV/cm). The histogram plots of the same are shown in Figures 4.21a, 4.21b, and 4.21c.

The histograms were fitted with the function e^{a+bx} and the values of (a, b) for 25 kV/cm, 30 kV/cm and 35 kV/cm were (-0.108 ± 0.062, -0.448 ± 0.021), (-0.467 ±

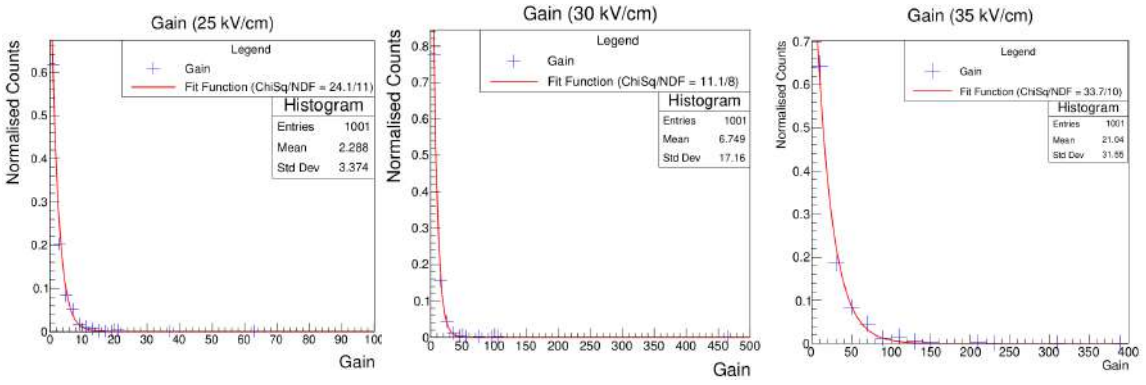

(a) (b) (c)

Figure 4.21: Histogram plots to calculate gain for three different fields across the Thick-GEM foil. The electric field in the drift and induction region were 2kV/cm.

0.056, -0.147 ± 0.006), and (-0.0229 ± 0.056, -0.0486 ± 0.0021) respectively, which correspond to a gain of about 2, 6 and 20 respectively. Owing to time constraints (the simulation for 35 kV/cm took about 25 days to complete), we could not proceed with simulating the same at higher voltages.

We see that the expected gain at 30 kV/cm match that of the prediction made in the previous section and that as we increase the field across the Thick-GEM holes, the gain increases. There is a limit of the fields we can reach as the capacitors in the low pass filters have a limit on the operating voltage. Increasing the electric field across the hole also leads to spurious signals as we will see in Section 4.13. Through simulations, we also observed a drop in the field uniformity across these holes as one increases the voltage. Figure 4.22a shows a contour plot of the electric field across the XY plane in the center of the Thick-GEM foil. We then stored the electric field across a line in the center of the hole parallel to the X-axis (See red line in Figure 4.22a). This was done for different field values across the Thick-GEM foil, and a plot of the same is shown in Figure 4.22b. We see that at higher fields, even though the correct bias is applied, there is a dip in the field at the center of the hole, which means that increasing voltage bias across the Thick-GEM foil layers does not correspond to a linear increase in the field at the center of the hole.

If the number of electrons generated in the drift volume and have reached the Thick-GEM hole is denoted as N_{hole} and the number of electrons generated in the drift volume is denoted as N_{drift}, then the collection efficiency is defined as:

$$\text{CE} = \frac{N_{\text{hole}}}{N_{\text{drift}}} \tag{4.1}$$

We require this value to be high as this ensures that all the electrons created in

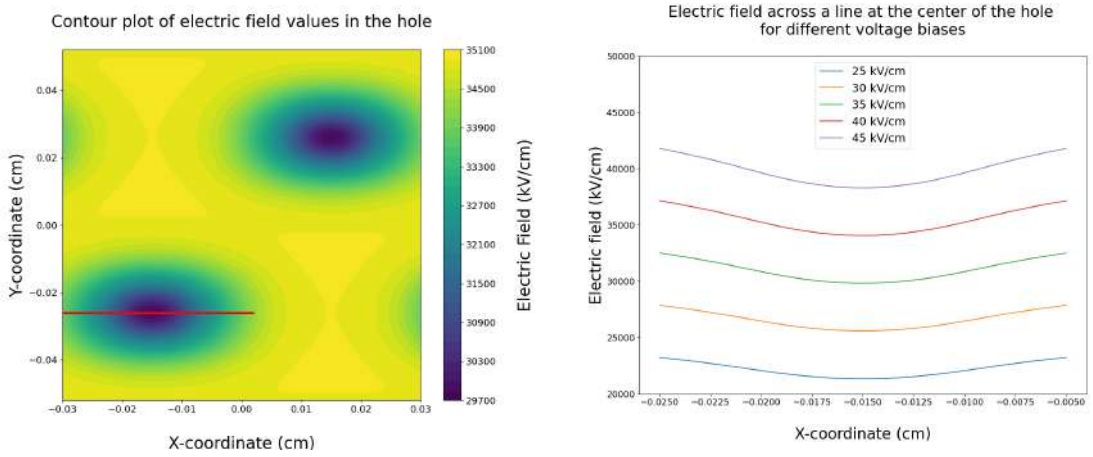

(a) (b)

Figure 4.22: (a) Contour plot of the electric field across the XY-plane in the center of the Thick-GEM foil (35kV/cm). (b) Electric field values across a line in the center of the hole parallel to the X-axis.

the drift volume are collected and sent drifting through the hole.

Apart from a high collection efficiency, we also need Extraction Efficiency (EE) to be high, where EE is defined as:

$$\mathrm{EE} = \frac{N_{\mathrm{hole}}}{N_{\mathrm{ind}}} \tag{4.2}$$

where N_{ind} is the number of electrons generated in the hole region and have reached the induction region.

CE and EE get us to the effective gain of the detector (G_{eff}), which is defined as:

$$G_{\mathrm{eff}} = G \times \mathrm{CE} \times \mathrm{EE} \times N_{\mathrm{primary}} \tag{4.3}$$

where G is the ideal gain of the detector and N_{primary} is the number of primary electrons generated in the detector volume. Maximizing CE gets us to a low EE (and thus low G_{eff}, and maximizing EE gets us to a low CE (and thus low G_{eff}). We thus need to operate the detector where the product of CE and EE is maximum.

Through simulations is the variation of CE and EE with $E_{\mathrm{drift}}/E_{\mathrm{hole}}$, where E_{drift} is the electric field in the drift region and E_{hole} is the electric field in the hole region. A plot of the same is shown in Figure 4.23.

Using the above results from simulations, we operated the detector at voltages that we expect to give the best gains. The expected amplitude of the signal we expect from the preamplifier is of the order of 1 mV, whereas we are currently getting

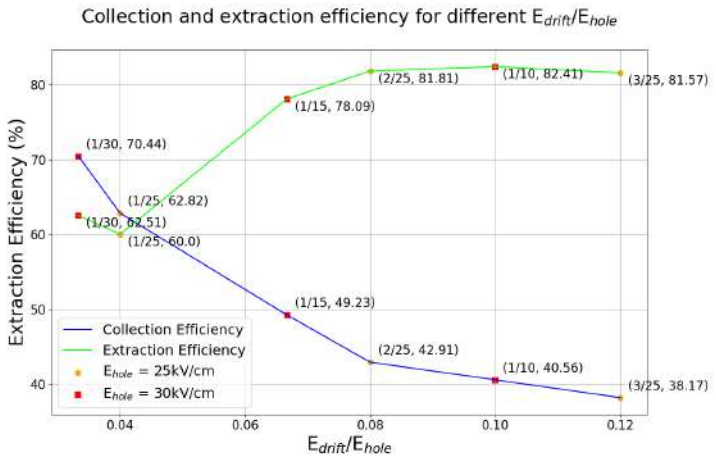

Figure 4.23: A plot of collection and extraction efficiency for different $E_{\text{drift}}/E_{\text{hole}}$ values. This simulation was done for two different E_{hole} values (25 and 30 kV/cm) and three different E_{drift} values (1, 2, and 3 kV/cm).

a noise of about ∼200 mV (See Figure 4.25), which is too high for the signal we are expecting, thus establishing a severe need to find ways to reduce noise or increase the gain of the detector.

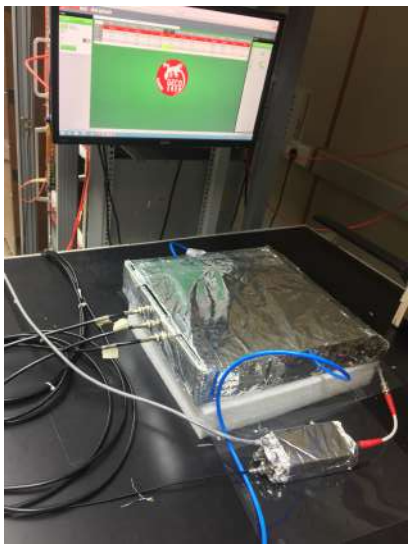

(a)

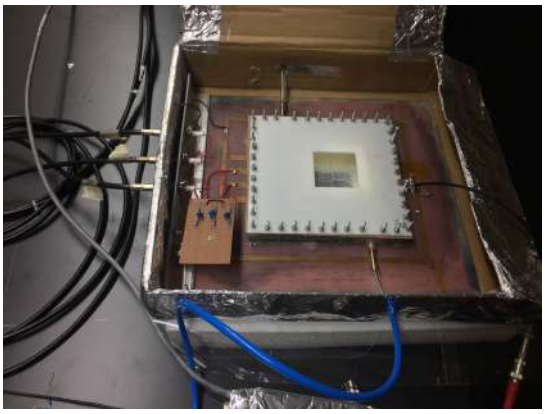

(b)

Figure 4.24: (a) An image of the detector inside the Faraday's cage. (b) An view of the detector inside the Faraday's cage.

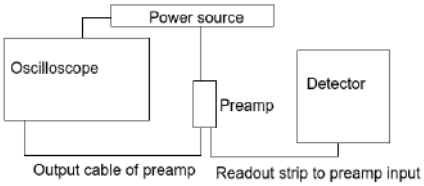

(a)

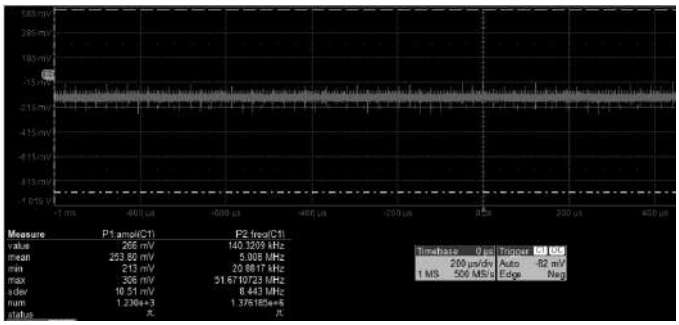

(b)

Figure 4.25: (a) The schematic circuit diagram to measure noise from the preamplifier connected to readout strips of the detector and (b) the corresponding output of the preamplifier.

4.12 Noise Reduction

As explained in the previous section, we believe that the expected signal from the ^{55}Fe source is much lower than compared to the noises we are observing. We can proceed further by either reducing the noise or increasing the signal amplitude (by increasing the effective gain of the detector).

One can observe an outer rectangular copper strip provided in Figure 4.5. This connection was made to provide points for ground connections. All grounds were made common using this strip, including the HV supply ground and the connection from the readout strip. But with a signal containing charges of the order of fCs, a disturbance in the ground[7] can affect the signal and induce noise. For this reason, we need to build a separate ground point using a large metallic plate or a very long and thick wire bundle so that it can act as a secondary ground, and given that we know there would not be disturbances from other appliances in the building, this would serve as a stable ground for us. There was access to a chemical ground that was utilized for grounding the detectors.

The following steps were implemented, which had an effect on reducing the noise:

1. To reduce the effect of stray electromagnetic radiations on the detector output, a Faraday cage was built inside which the detector was placed. See Figures 4.24a and 4.24b.

2. We started grounding components to a chemical ground using thick Aluminum braids. We grounded the preamplifier connections, high-voltage connections,

[7]This ground is the same one used for all ground connections in the building. Thus other appliances connected to this ground can alter the ground levels.

and the ground of the detector to the chemical ground. This brought down the noise from 200 mV to about 15 mV (See Figure 4.27a).

3. Finally, some minor tweaks were done to help with noise reduction. The gas nozzles and the screws used to make the gas-tight detector were seen to act as antennas, so they were grounded. Additionally, grounding the preamplifier body and the Faraday cage helped in reducing the noise from 15 mV to around 6 mV (See Figure 4.27b).

An image of the setup after all the steps were implemented is shown in Figure 4.26.

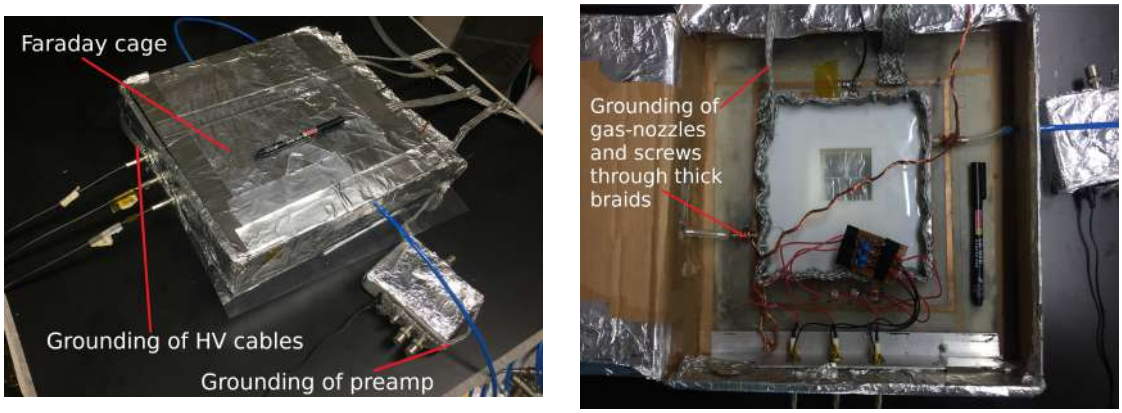

(a) (b)

Figure 4.26: Images of the detector setup after steps were taken to reduce noise.

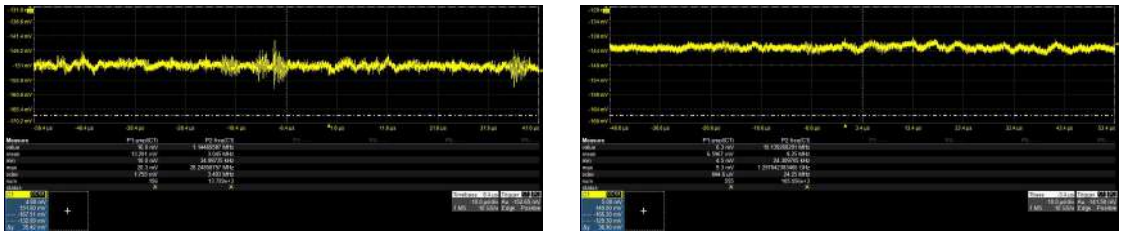

(a) (b)

Figure 4.27: Noise observed from the preamplifier at different stages of attempts to reduce the noise. A noise of about 15 mV is seen in (a) and about 6 mV in (b).

Finally, we also noted that the noise from the detector was of the order of 2 mV after all the steps were taken to reduce the noise, which means a good amount of noise is also being picked up by the preamplifier. An image showing the same is shown in Figure 4.28.

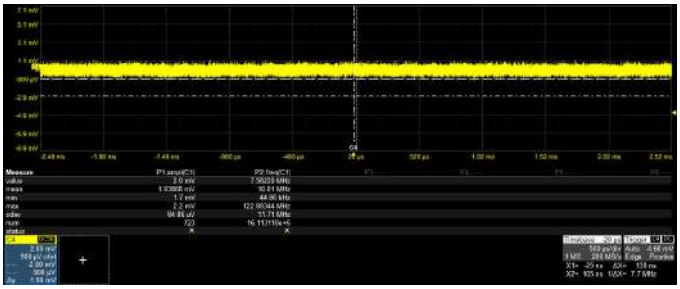

Figure 4.28: The noise observed from the detector (less than 2 mV). The circuit diagram of the setup in consideration would be similar to that of Figure 4.25a but with the detector output directly connected to the oscilloscope.

Looking at Figure 4.1, we have used low pass filters from a HV connection to each electrode, but another mode of operation is to use a HV divider circuit, which also did not help with reducing the noise or producing a signal.

The CAEN HV supply was upgraded from the previously used N1470 module to an N1471 module. The new module has a current resolution of 0.5nA, whereas the N1470 module has a resolution of 5nA. For this reason, using the new module to quantify the current leak in the High-voltage supply circuit is better than the N1470 module. The desired leak current in the high-voltage circuit is around 20nA. The initial leak current we observed was of the order of 200nA. After replacing the capacitors and resistors with new ones, soldering the circuit with lesser edges (to prevent discharges), and covering metallic ends with Kapton tape (an image of the end result is as seen in Figure 4.29a, we achieved an acceptable leak current for 500 V (See Table 4.5). The readings in Tables 4.5 and 4.5 show an ohmic behavior. The maximum voltage the capacitors and resistors can be operated is 3 kV, but the capacitors started sparking at around 2250V, which led us to ordering a better set of components.

V	I_1 (μA)	I_2 (μA)	I_3 (μA)
500	0.0338	0.0196	0.0655
750	0.0632	0.0348	0.1132
1000	0.094	0.0545	0.1724
1250	0.1252	0.0908	0.2313
1500	0.1653	0.1211	0.3182
1750	0.2077	0.1567	0.404
2000	0.261	0.203	0.5066
2250	—	Sparking	—

Table 4.4: The leak current in the circuits for the three terminals for the corresponding voltage applied. I_1, I_2, and I_3 correspond to the current in the lower Thick-GEM, upper Thick-GEM and drift electrode circuits, respectively.

(a) (b)

Figure 4.29: Images of (a) front side and (b) backside of the well-soldered and cleaned protective circuit made in a way to have minimum leakage in current.

V	I_1 (μA)	I_2 (μA)	I_3 (μA)
500	0.0034	0.0021	0.0149
750	0.0065	0.0029	0.0228
1000	0.0099	0.0055	0.0371
1250	0.0138	0.0068	0.0481
1500	0.018	0.01	0.0657

Table 4.5: The leak current in the circuits after careful construction and precautions. An image of the corresponding circuit is as seen in 4.29.

4.13 Increasing Signal Amplitude

We have three Thick-GEMs of only one configuration (different specifications give different gains). There are three ways to increase the gain of the detector:

1. By changing the gas mixtures: Lesser amounts of quenching gas would mean greater amplification. Until now, we have tried three different gas mixtures: Ar-CO_2 (70%-30%), Ar-CO_2 (80%-20%), and Ar-CH_4 (90%-10%), and we went up to high fields too, all giving no observable signal from the ^{55}Fe source.

2. Using multiple Thick-GEM foils to increase the gain of the detector: This is done by stacking multiple foils, one above the other, with the readout and drift electrode at the bottom and top, respectively, as usual. But the etching process

we did had four electrodes included that can be used to provide a bias to the electrodes inside the gas-tight setup. For housing multiple Thick-GEM foils, we would need to etch a new board and thus a restart of the entire detector fabrication process, which was difficult in the given time frame.

3. Increasing the electric field.

In an attempt to increase the amplification by increasing the electric field in the Thick-GEM foil and thus the signal amplitude, we observed signals at electric fields higher than 3 kV/cm, 26 kV/cm, and 4 kV/cm in the induction, Thick-GEM hole, and drift regions respectively. Figure 4.30 shows the oscilloscope output of the preamplifier with an ^{55}Fe source, which is promising. One observation is that the signal amplitude is in the order of volts, which means the number of charges going into the preamplifier from the readout is too high. We conjectured that the source of this signal was cosmogenic backgrounds like muons (usually of the order of GeVs). Two arguments can disprove this conjecture:

- The rate of muons hitting the surface of the Earth is around 1 /cm^2/min[8]. The rate at which we were observing the pulses was around 6 /cm^2/min.
- Even if we assume that these pulses were being produced due to cosmogenic muons, which means that the detector is working, why is the source almost invisible to the detector output (no difference in the pulse count irrespective of the source being placed or not)?

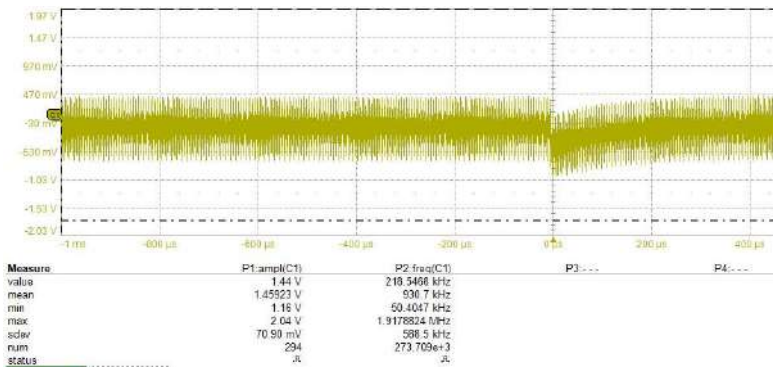

Figure 4.30: The preamplifier output of the detector with source placed.

Another interesting problem we encountered is the observation of large signals with and without the presence of the ^{55}Fe source. We observed these pulses only at higher fields in the detector, which means that these are just spurious signals.

[8]Source: The Berkeley Lab Cosmic Ray Telescope Project

The drift electrode was made using Aluminum tape, which is about 5 cm wide. Since the working area of the drift electrode is 10×10 cm^2, we needed to use the tape twice to cover the entire area. The line where this joint is made, would have an edge, around which the electric field would be huge and can act as a source for ionizations. The Thick-GEM holes were made using a mechanical drill, unlike a chemical etching process for GEM holes. This allows the possibility of sharp cuts or protrusions in the copper layers, thus again acting as a source for ionizations.

Chapter 5

Development of the Proportional Counter

5.1 Overview

This Chapter will deal with the details of the work done to fabricate and characterize a proportional counter and discuss the results obtained from a few simulations performed using Garfield++. The testing process of the Thick-GEM, as we saw in Chapter 4 requires effectively extracting pulses of charges of low magnitude and, at the same time, minimizing noise to the Femto-coulomb or sub-Femto-coulomb range. The motive to make and test a detector like a proportional counter is to introduce the importance of gain and noise reduction. The Thick-GEM detector is susceptible to noise and the charge of noise pulses is in the Femto coulomb range. In contrast, the proportional counter can achieve high gains with similar voltage biases applied. Making the proportional counter work also gave us another handle to test the electronic chain.

The proportional counter comprises a thin anode wire, a grounded cylinder circumscribing this wire, and a window transparent to incoming particles. There is a gas mixture flowing inside the detector volume. P-10 gas (Ar+CH_4 (90%+10%)) was the gas that was used. The electric field inside the proportional counter is as given in Equation 3.5. As one gets closer to the anode wire, the electric field magnitude increases, and the avalanches occur around the wire. The following components are needed to construct the detector fully:

- Outer Cylinder
- Thin anode wire
- End caps for gas-tight connection
- Electronics

5.2 Design and Fabrication

The proportional counter is a simple detector to fabricate. The only challenge is to have a tight wire inside the cylinder while maintaining a gas-tight setup with the end

caps. We cut an Aluminum tube to make the outer cylinder, a copper strand that can be found in regular wires as the anode wire, and a 3D printed component as the end caps.

The outer cylinder was from an Aluminum tube of diameter 1.9 cm, and the length of the cut tube was 15 cm. A small rectangular window was cut using a drill with a cutting disk in this outer cylinder. To make the cylinder gas-tight, we used Kapton tape to cover this window, through which the incident radiation enters.

The end caps were designed on AutoCAD and printed using the 3D printer available in the Robotics Laboratory at NISER. These caps also had two tubes protruding to serve as the inlet and outlet pipes for the gas to flow through. Images of the same are shown in Figures 5.1a and 5.1b.

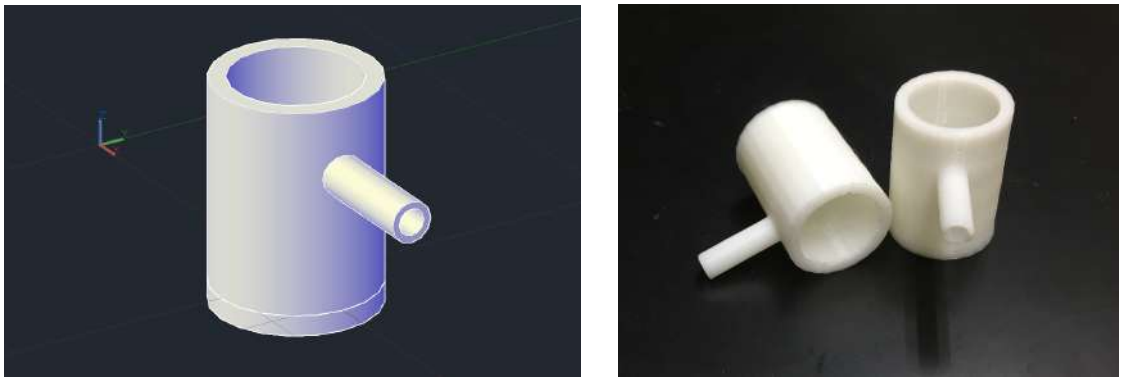

(a) (b)

Figure 5.1: Image of (a) the end cap designed on AutoCAD and (b) the 3D printed end caps.

The anode wire taken from the copper strands present in regular wires was of thickness 0.027 cm. There were no holes made in the end caps so that the wire could go through as the printer does not have the capabilities of printing objects of dimensions of 0.05 mm order. But one important process for a 3D printer to work is that the resin is melted and molded into shapes, which is what makes the printer create objects of the desired designs and shapes. This meant that we could heat the wire and make it pass through the end caps through a hole of the size of its diameter. We applied glue on the outside to ensure there was no leak. The wire coming out was then connected to the preamplifier (through an SHV connector) and further electronics. An image of the detector at this stage is shown in Figure 5.2a.

The electronics chain is exactly the same as that of the Thick-GEM, i.e., we have used a 142IH Ortec preamplifier, a CAEN N968 Spectroscopy Amplifier, and an Ortec 927 ASPEC MCA.

Although the proportional counter has a high gain, the noises we were initially

observing were very high and were a 50 Hz noise from some electrical component in the building. To reduce the same, we grounded the outer body of the preamplifier and made a Faraday cage that housed the proportional counter. An image of the same is shown in Figure 5.2b. This was sufficient to bring down the noises to a level where we could observe the signal. This shows how careful one needs to be while operating a Thick-GEM detector compared to the proportional counter.

(a) (b)

Figure 5.2: An image of (a) the proportional counter built and (b) the detector placed in a Faraday cage.

5.3 Initial Checks

For a voltage of 2800 V supplied to the anode wire, and after placing an ^{55}Fe source, we observed the outputs of the preamplifier, the amplifier, and the MCA output. The same has been shown in Figures 5.3a, 5.3a and 5.4.

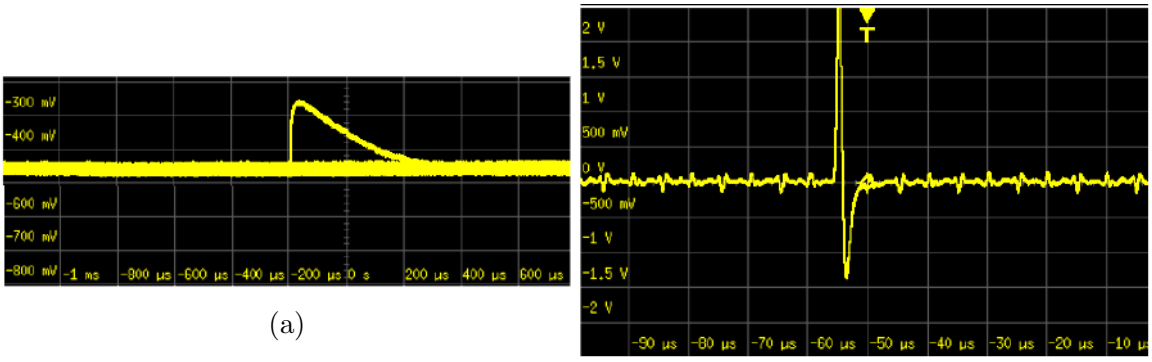

(a) (b)

Figure 5.3: For an ^{55}Fe source, the output from the (a) preamplifier and (b) amplifier that was observed with an oscilloscope. Here the X-Axis is the time, and the Y-Axis is the voltage.

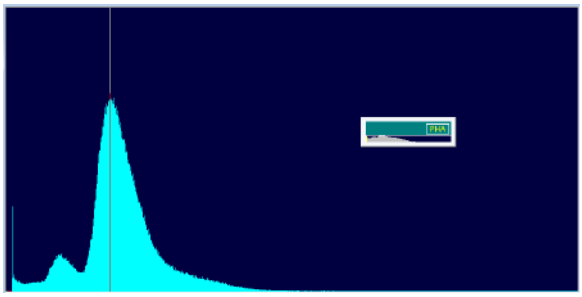

Figure 5.4: The MCA output for an ^{55}Fe source placed in front of the proportional counter. Here the X-Axis is the channel number, and the Y-Axis is the counts.

We observe that we have obtained the desired characteristic 5.9 keV peak of the Iron source and the Argon escape peak to the left. We now will move forward to performing a characterization of the proportional counter.

5.4 Characterization

For the main peak in the spectrum, the Full-Width at Half Maximum (FWHM) which is related to the standard deviation by:

$$\text{FWHM} = 2 \times \sqrt{2 \times \ln(2)} \times \sigma \tag{5.1}$$

where σ is the standard deviation of the Gaussian.

Using FWHM, one defines resolution, given by:

$$\text{Resolution } (\%) = \frac{\text{FWHM}}{E} \tag{5.2}$$

where E is the related energy of the peak and corresponds to the peak centroid in the MCA output.

It is desirable that a detector is operating in a configuration with the least resolution. The resolution varies with the voltage supplied to the anode wire for proportional counters. After placing the source, we obtained the spectra for a specific voltage and subtracted them from the spectra obtained without the source (background). This was done for different voltages, thus giving us a plot of resolution vs. voltage supplied to the anode wire. The plot of the same is shown in Figure 5.5.

We see that the proportional counter we built performs best when a voltage of 2670V is given to the anode wire. For voltages beyond 2850V, we observed sparks in the proportional counter, and an image of the same is shown in Figure 5.6.

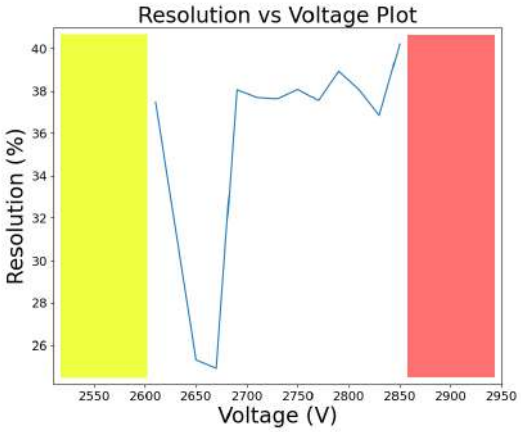

Figure 5.5: The plot of resolution vs. voltage applied to the anode wire. The yellow box corresponds to the region where the voltage supplied is too low for the peak to be resolved, and the red box corresponds to the region where the voltage supplied is too high, leading to sparking.

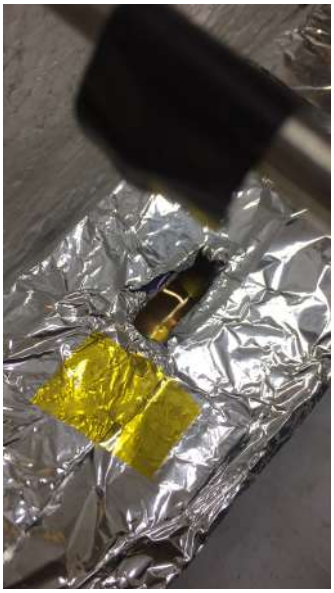

Figure 5.6: An image captured when the proportional counter was sparking.

5.5 Operating at Negative Voltage

Proportional counters always have a positive voltage to the anode wire and grounded outer cylinder. Let us refer to this configuration as the positive-voltage configuration. One question to ask is why is it always in this configuration (a positive voltage to the

anode and grounding of the cylinder)?

Suppose one grounds the anode wire and a positive voltage to the cylinder. In that case, the electric field inside will not reach the required levels to produce sufficient multiplication for a readable output. This can be done through a simple calculation similar to what was done to derive Equation 3.5.

Let us refer to the setup wherein the anode wire is given a negative voltage (and the cylinder grounded) as the negative-voltage configuration. The electric field magnitude would be the same but opposite in direction compared to that of the positive-voltage configuration. When an ionizing radiation enters the detector volume in the positive-voltage configuration, electrons drift towards the anode, and as they get closer, the field increases. The majority of the ions are formed near the wire, and they drift towards the cylinder walls; and given the slow speed of the ions and having to traverse a long distance, the pulse has a long tail. Appendix A.3 goes into the equations involved in the charge pulse output. It is desirable to have a short tail. Thus the advantage of operating the proportional counter in the negative-voltage configuration is that we predict a shortening of the pulse's tail as the ions will have to drift much smaller distances.

Upon testing the same, we got no signal, as shown in Figure 5.7. The expected gain in this mode of operation is expected to be low and hence not producing a large signal compared to what was produced in the positive-voltage configuration. This is because in the positive-voltage configuration, as the primary electrons drift towards the wire and hence higher fields, they ionize further atoms, electrons from which ionize further atoms, and so on. In the negative-voltage configuration, the electrons drift towards the cylinder and towards regions where the field is lower, thus not giving rise to a big enough avalanche effect to produce a readable signal.

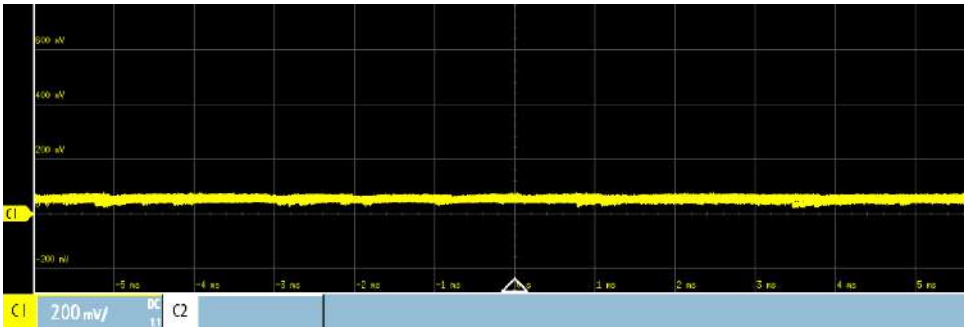

Figure 5.7: For an ^{55}Fe source, the preamplifier output of the proportional counter in the negative-voltage configuration. Here the X-Axis is the time, and the Y-Axis is the voltage.

To confirm the statement made in the previous paragraph, we simulated a proportional counter similar to what was used in the experiment using Garfield++ and the

neBEM package. There is no tube-like structure in the geometries that neBEM can discretize, instead, we made a cuboid structure instead of the outer cylinder. neBEM does have a pre-defined wire geometry and we used one that is exactly similar to that of the one used in the experiment. We simulated the gain for both the negative and positive-voltage configuration for 1000 events. Here one event corresponds to an electron left in the drift medium. The results of the same are shown in Figures 5.8a and 5.8b. The histograms were fitted with the function e^{a+bx} and the values of (a, b) for the positive and negative-voltage configurations were (-0.29 $\pm$ 0.053, -(234.3 $\pm$ 9.5)$\times 10^{-6}$) and (0.109 $\pm$ 0.057, -0.0922 $\pm$ 0.004) respectively, which correspond to a gain of about 4200 and 2 respectively. The gain for the positive-voltage configuration is three orders higher than that of the negative-voltage configuration, which confirms the statement made in the previous paragraph.

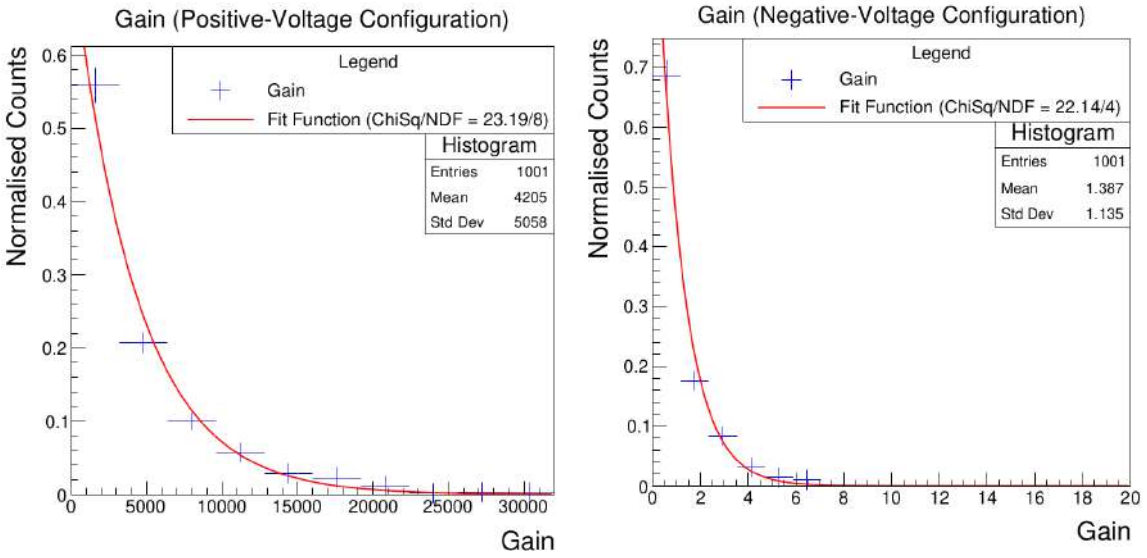

(a) (b)

Figure 5.8: The distributions of gain for 1000 events for (a) positive and (b) negative voltage configurations.

As seen through simulations and experiments, the gain of the proportional counter is typically of the order of 10^3 and that of Thick-GEMs is around 10^2, which means that one has to look at noise more carefully in a Thick-GEM compared to the proportional counter. The electric field in the holes of the Thick-GEM are governed by the foil thickness and the voltage bias applied, whereas the electric field near the wire in a proportional counter can reach very high values. Another advantage of the proportional counter is that it has a reduced ion-backflow and there is almost no trapping of ions that can distort the electric field, as it occurs in Thick-GEMs. But the

proportional counter is a detector that can easily shift to working in the GM region, depending on the voltage bias applied, whereas this is not the case in Thick-GEMs.

5.6 Gain Evolution in a Proportional Counter

Another interesting study that was done with the proportional counter was to see the effect of long time exposure to the ^{55}Fe source on the detector gain. We left the detector running for 16 hours, with the MCA running on a macro. The macro code commanded the MCA to take the spectrum data for 59 seconds and save the spectrum in a file. The data-taking process would again begin once the next minute begins. This was done for 999 minutes, amounting to about 16 hours' worth of data-taking. The MCA output was calibrated using a test pulse generator and given we approximately find the number of primary ionizations produced in the volume (similar to calculations done in Section), we can relate the channel number to the charge of the signal pulse. We found that for the setup we used, charge generated = 0.056×Channel_No. + 0.467 (fC). By a simple calculation, we can calculate the expected number of primary electrons produced (= 0.039 fC), and we can thus obtain the gain of the detector for every minute of the data-taking process. This results in a plot of gain vs. time (See Figure 5.9).

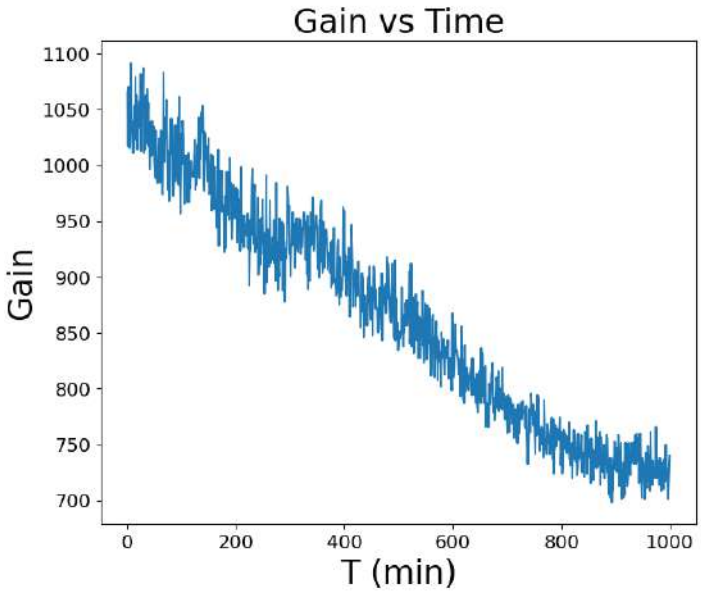

Figure 5.9: A plot of gain vs. time to demonstrate the drop in gain in the proportional counter upon continuous radiation exposure.

We see that the gain value drops over a period of 16 hours, and this drop can be due to charging up and changes in temperature and pressure.

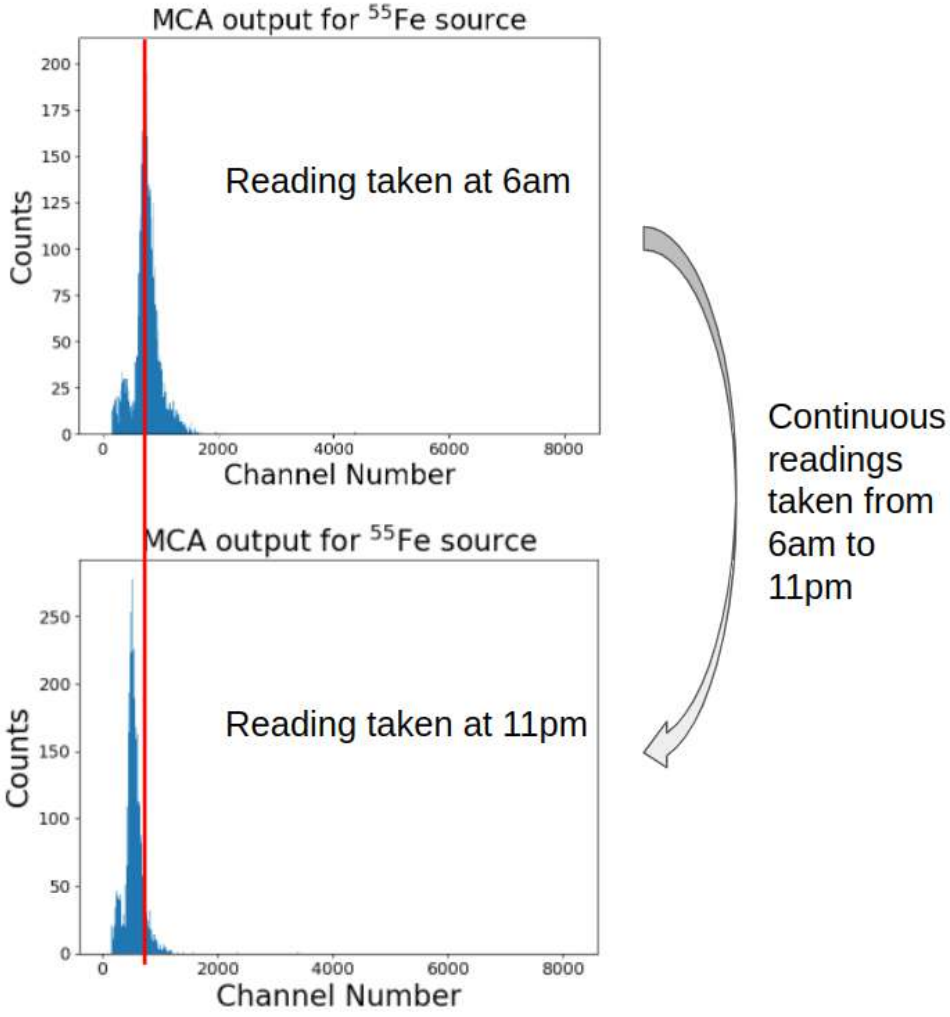

Figure 5.10: The shift in peak for spectrums obtained at two different times during the continuous exposure to radiation. The shift in centroid shows the drop in the detector gain over time.

Chapter 6

Conclusion and Outlook

During the entirety of the academic year, the concepts of interaction of radiation and matter, and working principles of gaseous radiation detectors were learned. The skills pertaining to designing and fabricating a Thick-GEM detector from scratch was learned. We successfully constructed and assembled the detector to perform some preliminary tests, the observations of the same have been shown in Chapter 4. Owing to noise levels being higher than the expected signal, we have not observed any signal. Garfield++ simulations were performed to study the gain, field uniformity and collection and extraction efficiency, results of which can be used to find an optimum configuration to operate the detector in. The noise levels were brought down from 200 mV to 6 mV and the leak current was brought down to less than 20 nA for a supply of 500 V. We now predict that with a new detector capable of housing multiple Thick-GEM foils and having undergone the same steps we did to reduce noise, one can observe signals by reaching higher gains.

A proportional counter was built to show the ease in producing a signal with a detector capable of producing high gains, as compared to a sophisticated detector like the Thick-GEM. The success in producing a signal in the proportional counter also served as a check to show all the components in the electronics chain was working. The working principle of the proportional counter was better learned through Garfield++ simulations and by operating the detector with a negative bias to the anode wire. Finally, the evolution of gain of the detector over time when exposed to radiation continuously was studied.

Appendix A

Derivations

A.1 Bohr's Derivation of Energy Loss of Heavy Particles in Matter

Bohr derived the energy loss that an incident particle would experience when it traverses through some material medium. Let us say the incident particle has charge Ze, mass M and is traveling at a velocity v. The mass of an electron is labeled as m_e.

There are two important assumptions that Bohr makes:

1. M is large enough (M >> m_e) that it does not deviate from its path as it goes through the material.

2. The velocity of the incident particle, v, is much greater than that of the velocity of the bound electrons of the atoms in the medium. This assumption is made so that we further safely assume that these bound electrons are stationary with respect to the incident particle.

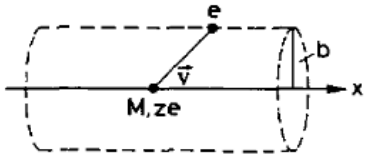

Figure A.1: Schematic diagram of the collision of the incident particle and an electron bound to the atoms of the material. Source: [12]

We now calculate the impulse imparted on an electron at some distance from the incident particle. The distance between these two particles along the z-direction is b, and can be seen in Figure A.1.

$$I = \int F dt = e \int E dt = e \int E \frac{dt}{dx} dx = e \int E \frac{dx}{v} = \frac{e}{v} \int E_{\perp} dx$$

where E is the total electric field of the incident particle and $E_{\perp}$is the perpendicular component. We do not have the parallel component ($E_{\parallel}$) because the values

of $e\int_{-\infty}^{c} E_{\parallel}dx$ and $e\int_{c}^{\infty} E_{\parallel}dx$ are equal and opposite in magnitude. Here c is the x-coordinate of the electron.

Considering an infinitely long cylinder of radius b, with the central axis along the incident particle trajectory. Using Gauss's Law, we get:

$$\int E_{\perp} 2\pi b dx = 4\pi z e \implies \int E_{\perp} dx = \frac{2ze}{b} \implies I = \frac{2ze^2}{bv}$$

Thus the energy gained by the electron, given by $\frac{I^2}{2m_e}$ is:

$$\Delta E(b) = \frac{2z^2e^4}{m_e v^2 b^2} \tag{A.1}$$

For N_e being the density of electrons in the medium, the incident particle loses energy to electrons present at a perpendicular distance between b to b + db in a thickness dx given by:

$$-dE(b) = \Delta E(b) N_e dV = \frac{4\pi z^2 e^4}{m_e v^2} N_c \frac{db}{b} dx \implies -\frac{dE}{dx} = \frac{4\pi z^2 e^4 n}{mv^2} \ln \frac{b_{\max}}{b_{\min}}$$

Instead of integrating the above quantity from $b_{min} = 0$ to $b_{max} = \infty$ is a wrong direction to proceed in. This is because, for very large b, the collisions do not occur instantly, thus making the impulse calculations invalid. Additionally, the above equation becomes infinite after setting $b_{min} = 0$.

To obtain the lower limits of the integration b_{min}, we consider the maximum energy transfer possible in a head-on collision. This corresponds to the electron obtaining energy of $\frac{1}{2}m_e(2v)^2$, which can be derived from the kinematic calculations of elastic collisions between a massive particle and a particle with much lower mass. When relativity is taken into account, the value has to be changed to $2\gamma^2 mv^2$, where $\frac{v}{c}$ and $\gamma = \frac{1}{\sqrt{1-\beta^2}}$. Plugging this loss in energy in Equation A.1, we get:

$$b_{min} = \frac{ze^2}{\gamma m_e v^2}$$

To calculate the value of b_{max}, we consider the orbital frequency ν of the bound electrons in the medium. As explained in [12], the impulse transfer should happen in a short time compared to the time period of the bound electron, $\frac{1}{\nu}$. For our collisions, the typical interaction time is given by $t = \frac{b}{v}$, which after accounting for relativity, becomes $\frac{b}{\gamma v}$, so that

$$\frac{b}{\gamma v} \leq \tau = \frac{1}{\bar{\nu}}$$

Considering that there are several bound electrons with different frequencies, we have replaced ν with the mean frequency, $\overline{\nu}$.

Thus, substituting b_{max} and b_{min}, we get the Bohr's classical formula:

$$-\frac{dE}{dx} = \frac{4\pi z^2 e^4}{m_e v^2} N_e \ln \frac{\gamma^2 m v^3}{z e^2 \overline{\nu}} \tag{A.2}$$

A.2 Interaction Probability and Mean Free Path

Let us consider a slab of matter with thickness x. We want to calculate the probability for the interaction of a particle traveling through this slab containing many interaction centers. As explained in [12], let $P(x)$ be the probability of not having an interaction after a distance x, and wdx be the probability of having an interaction between x and $x + dx$. The probability of not having an interaction between x and $x + dx$ is given by:

$$\begin{aligned} & P(x + dx) = P(x)(1 - wdx) \\ & P(x) + \frac{dP}{dx}dx = P(x) - P(x)wdx \text{ (by first order approximation)} \\ \implies & dP(x) = -wP(x)dx \implies P = C\exp(-wx) \end{aligned}$$

where C is a constant of integration. After imposing $P(0) = 1$, we obtain $C = 1$.

The mean distance travelled by the particle without suffering a collision (λ), or generally known as the mean free path can be calculated using P(x) and is thus found using the relation:

$$\lambda = \frac{\int xP(x)dx}{\int P(x)dx} = \frac{1/w^2}{1/w} = \frac{1}{w} \tag{A.3}$$

A.3 Signal Induced in a Proportional Counter

Consider a proportional counter with an anode wire of radius a and a potential V through a resistance R. The outer cylinder of radius b is grounded. The electric field at a radial distance r measured from the axis is given by

$$E(r) = \frac{V}{r \ln\left(\frac{b}{a}\right)}$$

As explained in [11], we will be calculating the pulse shape $V(t)$ due to induced charge resulting from the motion in the electric field of, say, N electron-ion pairs initially formed at the point r_0.

Before we proceed, we first need to find the induced charge at the anode from the electron collection. The N electrons and ions that were generated will drift in the electric field towards their respective electrodes, which leads to a transient current that will flow in the external circuit. We will calculate the contribution of each type of carrier to the total current from the conservation of energy. Looking at electrons: the rate dt/dt of energy gained by the electrons is given by: $\frac{d\epsilon}{dt} = NeE\frac{dx}{dt} = -Ne\frac{dV}{dx}.\frac{dx}{dt}$ $= -Ne\frac{dV}{dt}$ where $\frac{dV}{dt}$ is the rate of change of potential at the location of the electrons due to their drift in the electric field, and V and E are the potential and electric field at a point x respectively.

If C is the capacitance of the detector system, the fully charged system has a stored electrostatic energy of $Q^2/2C$. We also know that $\frac{d\epsilon}{dt} = \frac{d}{dt}\left(\frac{Q^2}{2C}\right) = V.i$, where i is the current flowing in the external circuit due to the motion of the electrons.

From these two equations, we can obtain i and the time integral of which will give us (the change in the induced charge at the anode from the electron collection):

$$q^{-} = \int i \cdot dt = -Ne \cdot \frac{\Delta V}{V} \tag{A.4}$$

where $\frac{\Delta V}{V}$ is the fraction of the total potential on the system, through which the electrons move before collection, and q^{-} is the induced charge at the central electrode due to the motion of electrons.

The second part of the calculation is to calculate the time (t_e) for electrons to arrive at the central wire:

$$t_e = \int_{r_0}^{a} -\frac{dr}{v_e(r)}$$

where v_e is the drift velocity of the electrons.

Equation 3.2 tells us that the electron drift velocity is proportional to $E^{1/2}$, i.e.

$$v_e = \mu\left(\frac{X}{p}\right)^{1/2} = kr^{-1/2}$$

where $k = \mu\left(\frac{V}{p\ln(b/a)}\right)^{1/2}$

Thus, the time for an electron initially at r_0 to arrive at the central wire is given by:

$$t_e = \int_{r_0}^{a} -\frac{dr}{v_e(r)} = \frac{2}{3k}\left(r_0^{3/2} - a^{3/2}\right)$$

Now we have all information to perform the final calculation. Let us say that the induced charges at the central electrode due to the motion of electrons and positive ions during the time t are $q^{-}$and q^{+} respectively (such that $0 < t \leqslant t_e$). Using

Equation A.4, we get:

$$q^{-}(t) = \frac{-Ne \ln \frac{r_0}{r_e}}{\ln \frac{b}{a}}$$

$$q^{+}(t) = \frac{Ne \ln \frac{r_0}{r_i}}{\ln \frac{b}{a}}$$

where r_e and r_i are the position of electrons and ions at time t, respectively.

For electron collection, we have:

$$q\left(t_e\right) = q^{-}\left(t_e\right) + q^{+}\left(t_e\right) = \frac{-Ne}{\ln \frac{b}{a}} \cdot \ln \frac{r_i}{a}$$

$$V\left(t_e\right) = \frac{q\left(t_e\right)}{C} = \frac{-Ne}{C \ln \frac{b}{a}} \ln \frac{r_i}{a}$$

Since the distance moved by the ions during electron collection is negligibly small, at $t_e,\ r_i \simeq r_0$. Thus the maximum pulse height reached during electron collection is:

$$V\left(t_e\right) \simeq \frac{-Ne}{C \ln \frac{b}{a}} \cdot \ln \frac{r_0}{a}$$

Appendix B

The Code for Simulating the Thick-GEM Detector on Garfield++

Listing B.1: Thick-GEM simulations using Garfield++

```
#include <iostream>
#include <TApplication.h>
#include <fstream>

#include "Garfield/SolidBox.hh"
#include "Garfield/SolidHole.hh"
#include "Garfield/SolidTube.hh"
#include "Garfield/SolidRidge.hh"
#include "Garfield/GeometrySimple.hh"
#include "Garfield/MediumMagboltz.hh"
#include "Garfield/MediumConductor.hh"
#include "Garfield/MediumPlastic.hh"
#include "Garfield/ComponentNeBem3d.hh"
#include "Garfield/ViewGeometry.hh"
#include "Garfield/ViewField.hh"
#include "Garfield/Random.hh"
#include "Garfield/Sensor.hh"
#include "Garfield/AvalancheMC.hh"
#include "Garfield/AvalancheMicroscopic.hh"
#include "Garfield/TrackHeed.hh"
#include "Garfield/ViewDrift.hh"
#include "Garfield/ViewSignal.hh"

using namespace std;
using namespace Garfield;

int main(int argc, char * argv[]) {

  TApplication app("app", &argc, argv);
```

```
30
31 // Define materials
32 // Gas mixture
33   MediumMagboltz *gas = new MediumMagboltz();
34   const double pressure = 760.;
35   const double temperature = 293.15;
36   gas->SetTemperature(temperature);
37   gas->SetPressure(pressure);
38   gas->SetComposition("Ar", 80., "CO2", 20.);
39   gas->LoadGasFile("../ar_80_co2_20_80k.gas");
40
41
42 // Read the ion mobility table from file.
43   //const string garfpath = getenv("GARFIELD_HOME");
44   gas->LoadIonMobility("/home/garfieldpp/Data/IonMobility_Ar+_Ar.txt")
45
46 // Other mediums
47   MediumConductor Cu;
48   MediumPlastic kp;
49   kp.SetDielectricConstant(3.9);
50
51 // Geometry.
52   GeometrySimple geo;
53   geo.SetMedium(gas);
54
55   double i_dia = 0.0200;
56   double o_dia = 0.0300;
57   double pitch = 0.0600;
58   double vpitch = sqrt(3)*pitch/2, hpitch = pitch/2;
59   double cu_height = 0.0005;
60   double kp_height = 0.0250;
61   double drift_gap = 0.5;
62   double ind_gap = 0.25;
63
64   double anode_z = 0.0 + cu_height/2;
65   double drift_z = anode_z + ind_gap + 2*cu_height +
       ↪ kp_height + drift_gap + cu_height;
66   double cu_upper_z = anode_z + ind_gap + cu_height +
       ↪ kp_height + cu_height;
67   double kapton_z = anode_z + ind_gap + cu_height +
       ↪ kp_height/2 + cu_height/2;
```

```
68  double cu_lower_z = anode_z + ind_gap + cu_height;
69
70  double position_x[3] = {-pitch, 0.0, pitch};
71  double position_y[3] = {-pitch, 0.0, pitch};
72
73  double driftV = -2500;
74  double upperV = -1500;
75  double lowerV = -500;
76  double anodeV = 0;
77  double field = (lowerV-upperV)/25;
78
79  double offset_x = 0.0, offset_y = 0.0, offset_z =
      ↪ 0.0;//cu_height/2 + kp_height/2;
80  double offset_x1 = -hpitch/2, offset_y1 = -vpitch/2,
      ↪ offset_z1 = 0.0;
81  double offset_x2 = +hpitch/2, offset_y2 = -vpitch/2,
      ↪ offset_z2 = 0.0;
82  double offset_x3 = +hpitch/2, offset_y3 = +vpitch/2,
      ↪ offset_z3 = 0.0;
83  double offset_x4 = -hpitch/2, offset_y4 = +vpitch/2,
      ↪ offset_z4 = 0.0;
84
85  std::cout<<"\nPitch = "<<pitch<<endl;
86
87  SolidBox drift(0.0, 0.0, drift_z, hpitch, vpitch,
      ↪ cu_height/2);
88  drift.SetBoundaryPotential(driftV);
89  geo.AddSolid(&drift, &Cu);
90
91
92
93  SolidHole cu_upper(0.0 + offset_x1, 0.0 + offset_y1,
      ↪ cu_upper_z, o_dia/2, o_dia/2, hpitch/2, vpitch/2,
      ↪ cu_height/2);
94  cu_upper.SetBoundaryPotential(upperV);
95  geo.AddSolid(&cu_upper, &Cu);
96
97  SolidHole kapton(0.0 + offset_x1, 0.0 + offset_y1,
      ↪ kapton_z, i_dia/2, i_dia/2, hpitch/2, vpitch/2,
      ↪ kp_height/2);
98  kapton.SetBoundaryDielectric();
```

```
99  geo.AddSolid(&kapton, &kp);
100
101 SolidHole cu_lower(0.0 + offset_x1, 0.0 + offset_y1,
      ↪ cu_lower_z, o_dia/2, o_dia/2, hpitch/2, vpitch/2,
      ↪ cu_height/2);
102 cu_lower.SetBoundaryPotential(lowerV);
103 geo.AddSolid(&cu_lower, &Cu);
104
105
106
107 SolidBox cu_upper2(0.0 + offset_x2, 0.0 + offset_y2,
      ↪ cu_upper_z, hpitch/2, vpitch/2, cu_height/2);
108 cu_upper2.SetBoundaryPotential(upperV);
109 geo.AddSolid(&cu_upper2, &Cu);
110
111 SolidBox kapton2(0.0 + offset_x2, 0.0 + offset_y2,
      ↪ kapton_z, hpitch/2, vpitch/2, kp_height/2);
112 kapton2.SetBoundaryDielectric();
113 geo.AddSolid(&kapton2, &kp);
114
115 SolidBox cu_lower2(0.0 + offset_x2, 0.0 + offset_y2,
      ↪ cu_lower_z, hpitch/2, vpitch/2, cu_height/2);
116 cu_lower2.SetBoundaryPotential(lowerV);
117 geo.AddSolid(&cu_lower2, &Cu);
118
119
120
121 SolidHole cu_upper3(0.0 + offset_x3, 0.0 + offset_y3,
      ↪ cu_upper_z, o_dia/2, o_dia/2, hpitch/2, vpitch/2,
      ↪ cu_height/2);
122 cu_upper3.SetBoundaryPotential(upperV);
123 geo.AddSolid(&cu_upper3, &Cu);
124
125 SolidHole kapton3(0.0 + offset_x3, 0.0 + offset_y3,
      ↪ kapton_z, i_dia/2, i_dia/2, hpitch/2, vpitch/2,
      ↪ kp_height/2);
126 kapton3.SetBoundaryDielectric();
127 geo.AddSolid(&kapton3, &kp);
128
129 SolidHole cu_lower3(0.0 + offset_x3, 0.0 + offset_y3,
      ↪ cu_lower_z, o_dia/2, o_dia/2, hpitch/2, vpitch/2,
```

```
    ↪ cu_height/2);
cu_lower3.SetBoundaryPotential(lowerV);
geo.AddSolid(&cu_lower3, &Cu);



SolidBox cu_upper4(0.0 + offset_x4, 0.0 + offset_y4,
    ↪ cu_upper_z, hpitch/2, vpitch/2, cu_height/2);
cu_upper4.SetBoundaryPotential(upperV);
geo.AddSolid(&cu_upper4, &Cu);

SolidBox kapton4(0.0 + offset_x4, 0.0 + offset_y4,
    ↪ kapton_z, hpitch/2, vpitch/2, kp_height/2);
kapton4.SetBoundaryDielectric();
geo.AddSolid(&kapton4, &kp);

SolidBox cu_lower4(0.0 + offset_x4, 0.0 + offset_y4,
    ↪ cu_lower_z, hpitch/2, vpitch/2, cu_height/2);
cu_lower4.SetBoundaryPotential(lowerV);
geo.AddSolid(&cu_lower4, &Cu);



SolidBox Anode(offset_x, offset_y, offset_z + anode_z,
    ↪ hpitch, vpitch, cu_height/2);
Anode.SetBoundaryPotential(anodeV);
Anode.SetLabel("anode");
geo.AddSolid(&Anode, &Cu);


//=================================================


// Plot device geometry in 3D
/*ViewGeometry geomView;
geomView.SetGeometry(&geo);
geomView.Plot();
app.Run();    // Keep this on to interact with the 3D
    ↪ figure
*/

```

```
165   // Plot device geometry in 2D
166   /*
167   ViewGeometry geomView2d;
168   geomView2d.SetGeometry(&geo);
169   geomView2d.SetArea(-2*pitch, -2*pitch, -10*kp_height,
        ↪ 2*pitch, 2*pitch, 5*kp_height);
170   geomView2d.SetPlane(0, 1, 0, 0, 0, 0.0);
171   geomView2d.Plot2d();
172   */
173
174   double tgtElSize = 1.e-2; // target element size -3
175   int minEl = 3, maxEl = 8; // minimum and maximum number
        ↪ of elements 3,11
176   int xcopy = 20, ycopy = 20, zcopy = 0;    // no. of
        ↪ copies in the 3 directions
177   ComponentNeBem3d nebem;
178   nebem.SetGeometry(&geo);
179   nebem.SetNumberOfThreads(32); // Set no. of threads for
        ↪ the calculation
180   nebem.SetTargetElementSize(tgtElSize);
181   nebem.SetMinMaxNumberOfElements(minEl, maxEl);
182   nebem.SetPeriodicityX(2*hpitch);
183   nebem.SetPeriodicityY(2*vpitch);
184   nebem.SetPeriodicCopies(xcopy, ycopy, zcopy);
185   nebem.UseLUInversion();
186 //  nebem.EnableDebugging();
187   nebem.Initialise();
188
189
190   cout<<endl<<"i_dia = "<<i_dia;
191   cout<<endl<<"o_dia = "<<o_dia;
192   cout<<endl<<"pitch = "<<pitch;
193   cout<<endl<<"vpitch = "<<vpitch;
194   cout<<endl<<"cu_height = "<<cu_height;
195   cout<<endl<<"kp_height = "<<kp_height;
196   cout<<endl<<"drift_gap = "<<drift_gap;
197   cout<<endl<<"ind_gap = "<<ind_gap;
198   cout<<endl<<"anode_z = "<<anode_z;
199   cout<<endl<<"drift_z = "<<drift_z;
200   cout<<endl<<"cu_upper_z = "<<cu_upper_z;
201   cout<<endl<<"kapton_z = "<<kapton_z;
```

```
202   cout<<endl<<"cu_lower_z = "<<cu_lower_z;
203
204
205
206   int plot_field = 0;
207   int calc_field = 0; // Save electric field/potential
        ↪ values in a file
208   int calc_ce = 1; // Calculate collection/extraction
        ↪ efficiency
209   int plot_drift_and_signal = 0; // Plot drift lines of
        ↪ electrons
210   int gain_calc = 0; // Calculate gain of the detector
211
212   if(plot_field==1){
213     std::cout<<"\n Potential plotting calculations have
          ↪ begun."<<endl;
214     ViewField fieldView;
215     fieldView.SetComponent(&nebem);
216     fieldView.SetNumberOfContours(20);
217     // Set the normal vector of the viewing plane (xz
          ↪ plane).
218     fieldView.SetPlane(0, -1, 0, +hpitch/2, +vpitch/2, 0);
219     // Set the plot limits in the current viewing plane.
220     fieldView.SetArea(-2*hpitch, cu_lower_z - 0.01,
          ↪ 2*hpitch, cu_upper_z + 0.01);
221     //fieldView.SetVoltageRange(-80000., 80000.);
222     TCanvas* cf = new TCanvas("cf", "Potential Plot
          ↪ (V/cm)", 600, 500);
223     //cf->SetLeftMargin(0.16);
224     fieldView.SetCanvas(cf);
225     fieldView.PlotContour("v");
226     char name0[1024];
227     sprintf(name0, "Potential_Plot_%dk.pdf", (int)field);
228     cf->SaveAs(name0);
229   }
230
231   if(calc_field==1){
232     std::cout<<"\n Field calculations have begun."<<endl;
233     {// field along line 1
234     std::ofstream fldfile;
235     char name1[1024];
```

```
236     sprintf(name1, "%dk_(%d, %d, %d,
           ↪ %d)_20x20_along_x(y=0.5drift_gap).csv",
           ↪ (int)field, (int)anodeV, (int)lowerV,
           ↪ (int)upperV, (int)driftV);
237
238     fldfile.open(name1);
239
240     int nx = 1000;
241     double delx = ((xcopy)*2*hpitch) / (double)(nx - 1);
242     double xp, yp = offset_y + vpitch/2, zp = offset_z +
           ↪ cu_upper_z + drift_gap/2;
243     Medium* medium = nullptr;
244     double ex = 0., ey = 0., ez = 0., e = 0.0, v = 0.;
245     int status = 0;
246     for(int ix = 0; ix < nx; ++ix){
247       xp = offset_x - (xcopy/2)*2*hpitch + ix*delx;
248       nebem.ElectricField(xp, yp, zp, ex, ey, ez, v,
             ↪ medium, status);
249       e = (ex*ex + ey*ey + ez*ez);
250       e = pow(e, 0.5);
251       fldfile << xp << "," << yp << "," << zp << "," <<
             ↪ ex << "," << ey << "," << ez << "," << e <<
             ↪ "," << v << "," << medium << "," << status <<
             ↪ std::endl;
252         }
253     fldfile.close();
254     }
255
256     {// field along line 2
257     std::ofstream fldfile;
258     char name2[1024];
259     sprintf(name2, "%dk_(%d, %d, %d,
           ↪ %d)_20x20_along_x(y=0.1_from_top_foil).csv",
           ↪ (int)field, (int)anodeV, (int)lowerV,
           ↪ (int)upperV, (int)driftV);
260
261     fldfile.open(name2);
262
263     int nx = 1000;
264     double delx = ((xcopy)*2*hpitch) / (double)(nx - 1);
```

```
265     double xp, yp = offset_y + vpitch/2, zp = offset_z +
          ↪ cu_upper_z + drift_gap/5;
266     Medium* medium = nullptr;
267     double ex = 0., ey = 0., ez = 0., e = 0.0, v = 0.;
268     int status = 0;
269     for(int ix = 0; ix < nx; ++ix)
270     {
271       xp = offset_x - (xcopy/2)*2*hpitch + ix*delx;
272       nebem.ElectricField(xp, yp, zp, ex, ey, ez, v,
            ↪ medium, status);
273       e = (ex*ex + ey*ey + ez*ez);
274       e = pow(e, 0.5);
275       fldfile << xp << "," << yp << "," << zp << "," <<
            ↪ ex << "," << ey << "," << ez << "," << e <<
            ↪ "," << v << "," << medium << "," << status <<
            ↪ std::endl;
276         }
277     fldfile.close();
278     }
279
280     {// field along line 3
281     std::ofstream fldfile;
282     char name3[1024];
283     sprintf(name3, "%dk_(%d, %d, %d,
          ↪ %d)_20x20_along_x(y=0.05_from_top_foil).csv",
          ↪ (int)field, (int)anodeV, (int)lowerV,
          ↪ (int)upperV, (int)driftV);
284     fldfile.open(name3);
285
286     int nx = 1000;
287     double delx = ((xcopy)*2*hpitch) / (double)(nx - 1);
288     double xp, yp = offset_y + vpitch/2, zp = offset_z +
          ↪ cu_upper_z + drift_gap/10;
289     Medium* medium = nullptr;
290     double ex = 0., ey = 0., ez = 0., e = 0.0, v = 0.;
291     int status = 0;
292     for(int ix = 0; ix < nx; ++ix)
293     {
294       xp = offset_x - (xcopy/2)*2*hpitch + ix*delx;
295       nebem.ElectricField(xp, yp, zp, ex, ey, ez, v,
            ↪ medium, status);
```

```
296         e = (ex*ex + ey*ey + ez*ez);
297         e = pow(e, 0.5);
298         fldfile << xp << "," << yp << "," << zp << "," <<
               ↪ ex << "," << ey << "," << ez << "," << e <<
               ↪ "," << v << "," << medium << "," << status <<
               ↪ std::endl;
299           }
300       fldfile.close();
301       }
302
303       {// field along line 4
304       std::ofstream fldfile;
305       char name4[1024];
306       sprintf(name4, "%dk_(%d, %d, %d,
             ↪ %d)_20x20_along_x(y=0.02_from_anode).csv",
             ↪ (int)field, (int)anodeV, (int)lowerV,
             ↪ (int)upperV, (int)driftV);
307       fldfile.open(name4);
308
309       int nx = 1000;
310       double delx = ((xcopy)*2*hpitch) / (double)(nx - 1);
311       double xp, yp = offset_y + vpitch/2, zp = anode_z +
             ↪ ind_gap/10;
312       Medium* medium = nullptr;
313       double ex = 0., ey = 0., ez = 0., e = 0.0, v = 0.;
314       int status = 0;
315       for(int ix = 0; ix < nx; ++ix)
316       {
317          xp = offset_x - (xcopy/2)*2*hpitch + ix*delx;
318          nebem.ElectricField(xp, yp, zp, ex, ey, ez, v,
                ↪ medium, status);
319          e = (ex*ex + ey*ey + ez*ez);
320          e = pow(e, 0.5);
321          fldfile << xp << "," << yp << "," << zp << "," <<
                ↪ ex << "," << ey << "," << ez << "," << e <<
                ↪ "," << v << "," << medium << "," << status <<
                ↪ std::endl;
322           }
323       fldfile.close();
324       }
325
```

```
326
327     {// field along line 5
328     std::ofstream fldfile;
329     char name5[1024];
330     sprintf(name5, "%dk_(%d, %d, %d,
          ↪ %d)_20x20_along_x(y=0.5ind_gap).csv",
          ↪ (int)field, (int)anodeV, (int)lowerV,
          ↪ (int)upperV, (int)driftV);
331     fldfile.open(name5);
332
333     int nx = 1000;
334     double delx = ((xcopy)*2*hpitch) / (double)(nx - 1);
335     double xp, yp = offset_y + vpitch/2, zp = cu_lower_z
          ↪ - ind_gap/2;
336     Medium* medium = nullptr;
337     double ex = 0., ey = 0., ez = 0., e = 0.0, v = 0.;
338     int status = 0;
339     for(int ix = 0; ix < nx; ++ix){
340       xp = offset_x - (xcopy/2)*2*hpitch + ix*delx;
341       nebem.ElectricField(xp, yp, zp, ex, ey, ez, v,
            ↪ medium, status);
342       e = (ex*ex + ey*ey + ez*ez);
343       e = pow(e, 0.5);
344       fldfile << xp << "," << yp << "," << zp << "," <<
            ↪ ex << "," << ey << "," << ez << "," << e <<
            ↪ "," << v << "," << medium << "," << status <<
            ↪ std::endl;
345         }
346     fldfile.close();
347     }
348
349     {// field along line 6
350     std::ofstream fldfile;
351     char name6[1024];
352     sprintf(name6, "%dk_(%d, %d, %d,
          ↪ %d)_20x20_along_x(y=0.05_from_bottom_foil).csv",
          ↪ (int)field, (int)anodeV, (int)lowerV,
          ↪ (int)upperV, (int)driftV);
353     fldfile.open(name6);
354
355     int nx = 1000;
```

```
356     double delx = ((xcopy)*2*hpitch) / (double)(nx - 1);
357     double xp, yp = offset_y + vpitch/2, zp = cu_lower_z
          ↪ - ind_gap/4;
358     Medium* medium = nullptr;
359     double ex = 0., ey = 0., ez = 0., e = 0.0, v = 0.;
360     int status = 0;
361     for(int ix = 0; ix < nx; ++ix)
362     {
363       xp = offset_x - (xcopy/2)*2*hpitch + ix*delx;
364       nebem.ElectricField(xp, yp, zp, ex, ey, ez, v,
            ↪ medium, status);
365       e = (ex*ex + ey*ey + ez*ez);
366       e = pow(e, 0.5);
367       fldfile << xp << "," << yp << "," << zp << "," <<
            ↪ ex << "," << ey << "," << ez << "," << e <<
            ↪ "," << v << "," << medium << "," << status <<
            ↪ std::endl;
368         }
369     fldfile.close();
370     }
371
372
373     {// field along line 7
374     std::ofstream fldfile;
375     char name7[1024];
376     sprintf(name7, "%dk_(%d, %d, %d,
          ↪ %d)_20x20_along_z.csv", (int)field, (int)anodeV,
          ↪ (int)lowerV, (int)upperV, (int)driftV);
377     fldfile.open(name7);
378
379     int nz = 1000;
380     double delz = (drift_z - anode_z) / (double)(nz - 1);
381     double xp = offset_x + hpitch/2, yp = offset_y +
          ↪ vpitch/2, zp;
382     Medium* medium = nullptr;
383     double ex = 0., ey = 0., ez = 0., e = 0.0, v = 0.;
384     int status = 0;
385     for(int iz = 0; iz < nz; ++iz)
386     {
387       zp = offset_z + anode_z + iz*delz;
```

```
388       nebem.ElectricField(xp, yp, zp, ex, ey, ez, v,
              ↪ medium, status);
389       e = (ex*ex + ey*ey + ez*ez);
390       e = pow(e, 0.5);
391       fldfile << xp << "," << yp << "," << zp << "," <<
              ↪ ex << "," << ey << "," << ez << "," << e <<
              ↪ "," << v << "," << medium << "," << status <<
              ↪ std::endl;
392     }
393     fldfile.close();
394     }
395   }
396
397
398   if(calc_ce == 1){
399     cout<<"\n Collection Efficiency calulcations have
          ↪ begun.\n";
400     int sensor_range = 5;
401     double xmin = -sensor_range * 2 * hpitch, ymin =
          ↪ -sensor_range * 2 * vpitch, zmin = 0.0;
402     double xmax = sensor_range * 2 * hpitch, ymax =
          ↪ sensor_range * 2 * vpitch, zmax = cu_upper_z +
          ↪ drift_gap;
403     // Create the sensor.
404     Sensor* sensor = new Sensor();
405     sensor->AddComponent(&nebem);
406     sensor->SetArea(xmax, ymax, zmax, xmin, ymin, zmin);
407     //sensor->AddElectrode(&nebem, "anode");
408     //sensor->AddElectrode(&nebem, "anode2");
409     std::cout << "Sensor has been created \n";
410
411     AvalancheMC aval;
412     aval.SetSensor(sensor);
413
414     /*AvalancheMC drift;
415     drift.SetSensor(sensor);
416     drift.SetDistanceSteps(2.e-2);*/
417
418     //ViewDrift* driftView = new ViewDrift();
419     //constexpr bool plotDrift = false;
420     //if (plotDrift) {
```

```
421       //aval.EnablePlotting(driftView);
422       //drift.EnablePlotting(&driftView);
423     //}
424
425     char collection_file[1024];
426     sprintf(collection_file, "CE_%dk_%fcm.csv",
            ↪ (int)field, drift_gap/2);
427     std::ofstream file;
428     file.open(collection_file);
429     file << "Event" << "," << "np" << "," << "j" << ","
            ↪ << "xe1" << "," << "ye1" << "," << "ze1" << ","
            ↪ << "xe2" << "," << "ye2" << "," << "ze2" <<
            ↪ std::endl;
430
431     int total = 0, up = 0, down = 0;
432
433     constexpr unsigned int nEvents = 1000;
434     for (unsigned int i = 0; i < nEvents; ++i) {
435       std::cout << "\n " << i+1 << "/" << nEvents << "\n";
436       const double x0 = offset_x3;
437       const double y0 = offset_y3;
438       const double z0 = cu_upper_z + drift_gap/2;
439       const double t0 = 0.;
440       const double e0 = 0.1;
441       aval.AvalancheElectron(x0, y0, z0, t0);
442       file << 0 << "," << 0 << "," << 0 << "," << x0 <<
            ↪ "," << y0 << "," << z0 << "," << 0. << "," <<
            ↪ 0. << "," << 0. << std::endl;
443       unsigned int ne = 0, ni = 0;
444       aval.GetAvalancheSize(ne, ni);
445       cout<<"\n Event = "<<i+1<<", Avalanche Size
            ↪ (electrons, ions) = ("<<ne<<", "<<ni<<")\n";
446       const unsigned int np =
            ↪ aval.GetNumberOfElectronEndpoints();
447       double xe1, ye1, ze1, te1, e1;
448       double xe2, ye2, ze2, te2, e2;
449       double xi1, yi1, zi1, ti1;
450       double xi2, yi2, zi2, ti2;
451       int status;
452       for (unsigned int j = 0; j < np; ++j) {
```

```
453         aval.GetElectronEndpoint(j, xe1, ye1, ze1, te1,
               ↪ xe2, ye2, ze2, te2, status);
454         file << i << "," << np << "," << j << "," << xe1
               ↪ << "," << ye1 << "," << ze1 << "," << xe2 <<
               ↪ "," << ye2 << "," << ze2 << std::endl;
455         if(ze1 > kapton_z){
456           total = total + 1;
457           if(ze2 > kapton_z){
458             up = up + 1;}
459           else if(ze2 < cu_lower_z - ind_gap/10){
460             down = down + 1;}
461         }
462         //drift.DriftIon(xe1, ye1, ze1, te1);
463         //drift.GetIonEndpoint(0, xi1, yi1, zi1, ti1,
               ↪ xi2, yi2, zi2, ti2, status);
464       }
465     cout<<"\nTotal = "<<total<<"\nUp = "<<up<<"\nDown =
        ↪ "<<down;
466     }
467
468     cout<<"\n::FINAL:: Total = "<<total<<"\nUp =
        ↪ "<<up<<"\nDown = "<<down;
469     file << total << "," << up << "," << down << "," << 0
        ↪ << "," << 0 << "," << 0 << "," << 0 << "," << 0
        ↪ << "," << 0 << std::endl;
470     //driftView->SetArea(xmax, ymax, zmax, xmin, ymin,
        ↪ zmin);
471     //driftView->SetPlane(0., -1., 0., 0., 0., 0.);
472     //TCanvas* cd = new TCanvas();
473     //driftView->SetCanvas(cd);
474     //driftView->Plot(0);
475     //cd->SaveAs("driftLines.pdf");
476     file.close();
477   }
478
479
480   if(plot_drift_and_signal == 1){
481     int sensor_range = 3;
482     double xmin = -sensor_range * 2 * hpitch, ymin =
        ↪ -sensor_range * 2 * vpitch, zmin = 0.0;
```

```
483     double xmax = sensor_range * 2 * hpitch, ymax =
          ↪ sensor_range * 2 * vpitch, zmax = cu_upper_z +
          ↪ drift_gap/5;
484     // Create the sensor.
485     Sensor* sensor = new Sensor();
486     sensor->AddComponent(&nebem);
487     sensor->SetArea(xmax, ymax, zmax, xmin, ymin, zmin);
488     sensor->AddElectrode(&nebem, "anode");
489     sensor->AddElectrode(&nebem, "anode2");
490     std::cout << "Sensor has been created \n";
491
492     // Create the charge multiplication method
493     AvalancheMC* avalMC = new AvalancheMC();
494     avalMC->SetSensor(sensor);
495     avalMC->EnableAvalancheSizeLimit(150);
496     avalMC->SetDistanceSteps(); // Use lower value for
          ↪ better precision
497     //avalMC->EnableSignalCalculation();
498
499     // HEED
500     TrackHeed* track = new TrackHeed();
501     track->SetSensor(sensor);
502     track->EnableElectricField();
503     track->SetParticle("mu");   // Incident particle
504     track->SetKineticEnergy(1.0e9); // Kinetic energy of
          ↪ the particle in eV
505
506     ViewDrift* driftView = new ViewDrift();
507     driftView->SetArea(xmax, ymax, cu_upper_z + 0.01,
          ↪ xmin, ymin, zmin);
508     driftView->SetPlane(0., -1., 0., 0., vpitch/2, 0.);
509     avalMC->EnablePlotting(driftView);
510     track->EnablePlotting(driftView);
511     TCanvas* cd = new TCanvas();
512     driftView->SetCanvas(cd);
513
514     const double tMin = 0.; // in ns
515     const double tMax = 100.;   // in ns
516     const double tStep = 0.05;  // in ns
517     const int nTimeBins = int((tMax - tMin) / tStep);
518     sensor->SetTimeWindow(tMin, tStep, nTimeBins);
```

```
519
520     float time[nTimeBins], current[nTimeBins];
521
522     // The initial position of the incoming ionising track
523     double track_x = offset_x3;
524     double track_y = offset_y3;
525     double track_z = cu_upper_z + drift_gap/10;
526
527     double t0 = 0;
528     double e0 = 0.1;
529     // Momentum direction of incoming track
530     float track_dx = 0.0;
531     float track_dy = 0.0;
532     float track_dz = -1.0;
533
534     int nEvent=3;
535
536     // Cluster info
537     double xcls, ycls, zcls, tcls, ecls, extra;
538     unsigned int ne, ni; // number of electrons in cluster
539     int nel, nend=0;
540     // Electron info
541     double xele, yele, zele, tele, eele, dxele, dyele,
          ↪ dzele;
542     int clust_id;
543
544     //If this drift plotting function does not work,
          ↪ start from the file with commit message "Checked
          ↪ drift lines for only-MC".
545
546     for(Int_t iEvent=0; iEvent<nEvent;iEvent++){
547       sensor->ClearSignal();    // Reset signals and free
            ↪ the sensor
548       track->NewTrack(track_x, track_y, track_z, tMin,
            ↪ track_dx, track_dy, track_dz);   // Incident
            ↪ particle track
549       bool clust_present=0;
550       clust_id = 0;
551       int p = 0;
552       do{   // Loop over all the cluster positions along
            ↪ the track
```

```
553         cout<<"Event = "<<iEvent+1<<": "<<"Cluster =
               ↪ "<<clust_id+1<<" :"<<endl;
554         clust_present=track->GetCluster(xcls, ycls, zcls,
               ↪ tcls, nel, ecls, extra);
555         p = p + nel;
556         for(int j = 0; j < nel; j++){   // Loop over all
               ↪ electrons in a cluster
557           track->GetElectron(j, xele, yele, zele, tele,
                 ↪ eele, dxele, dyele, dzele);
558           avalMC->AvalancheElectron(xele, yele, zele,
                 ↪ tele);
559           cout<<"\t j= "<<j+1<<"/"<<nel<<endl;
560         }
561         constexpr bool twod = true;
562         driftView->Plot(0);
563         //driftView->Plot(1);
564         //cd->Modified();
565         clust_id++;
566       }while(clust_present!=0);
567
568       int end=avalMC->GetNumberOfElectronEndpoints();
569       cout<<"\n Gain = "<<end<<endl;
570       cd->SaveAs("driftLines.pdf");
571       //driftView->Clear();
572     }
573   }
574
575   if(gain_calc == 1){
576     int sensor_range = 5;
577     double xmin = -sensor_range * 2 * hpitch, ymin =
           ↪ -sensor_range * 2 * vpitch, zmin = 0.0;
578     double xmax = sensor_range * 2 * hpitch, ymax =
           ↪ sensor_range * 2 * vpitch, zmax = cu_upper_z +
           ↪ drift_gap/4;
579     // Create the sensor.
580     Sensor* sensor = new Sensor();
581     sensor->AddComponent(&nebem);
582     sensor->SetArea(xmax, ymax, zmax, xmin, ymin, zmin);
583     //sensor->AddElectrode(&nebem, "anode");
584     //sensor->AddElectrode(&nebem, "anode2");
585     std::cout << "Sensor has been created \n";
```

```
586
587     // Create the charge multiplication method
588     AvalancheMC* avalMC = new AvalancheMC();
589     avalMC->SetSensor(sensor);
590     //avalMC->EnableAvalancheSizeLimit(150);
591     //avalMC->SetDistanceSteps();   // Use lower value
          ↪ for better precision
592     //avalMC->EnableSignalCalculation();
593
594     // The initial position of the incoming ionising track
595     double track_x = offset_x3;
596     double track_y = offset_y3;
597     double track_z = cu_upper_z + drift_gap/5;
598
599     double t0 = 0;
600     double e0 = 0.1;
601     // Momentum direction of incoming track
602     float track_dx = 0.0;
603     float track_dy = 0.0;
604     float track_dz = -1.0;
605
606     int nEvent=1000;
607
608     // Cluster info
609     double xcls, ycls, zcls, tcls, ecls, extra;
610     unsigned int ne, ni; // number of electrons in cluster
611     int nend=0;
612     // Electron info
613     double xele, yele, zele, tele, eele, dxele, dyele,
          ↪ dzele;
614     int clust_id;
615
616     std::ofstream file;
617     char gain_file[1024];
618     sprintf(gain_file, "Gain_%dk_%fcm.csv", (int)field,
          ↪ drift_gap/5);
619     file.open(gain_file);
620
621     for(Int_t iEvent=0; iEvent<nEvent;iEvent++){
622       avalMC->AvalancheElectron(track_x, track_y,
            ↪ track_z, t0, false);
```

```
623         ne = 0;
624         ni = 0;
625         avalMC->GetAvalancheSize(ne, ni);
626         nend = avalMC->GetNumberOfElectronEndpoints();
627         std::cout<<"\n\nEvent: "<<iEvent+1;
628         std::cout<<"\n\nGain from GetAvalSize(): "<<ne;
629         std::cout<<"\n\nGain from GetNo.ofEndPoints():
              ↪ "<<nend<<endl<<endl;
630         file << iEvent+1 << "," << ne << "," << nend <<
              ↪ std::endl;
631       }
632       file.close();
633     }
634
635     cout<<"\n\n :: Complete :: \n\n";
636     app.Run();
637     return 0;
638 }
```

Appendix C

The Code for Simulating the Proportional Counter

Listing C.1: Proportional counter simulations using Garfield++

```
1
2  #include <iostream>
3  #include <TApplication.h>
4  #include <fstream>
5
6  #include "Garfield/SolidBox.hh"
7  #include "Garfield/SolidHole.hh"
8  #include "Garfield/SolidTube.hh"
9  #include "Garfield/SolidWire.hh"
10 #include "Garfield/GeometrySimple.hh"
11 #include "Garfield/MediumMagboltz.hh"
12 #include "Garfield/MediumConductor.hh"
13 #include "Garfield/MediumPlastic.hh"
14 #include "Garfield/ComponentNeBem3d.hh"
15 #include "Garfield/ViewGeometry.hh"
16 #include "Garfield/ViewField.hh"
17 #include "Garfield/Random.hh"
18 #include "Garfield/Sensor.hh"
19 #include "Garfield/AvalancheMC.hh"
20 #include "Garfield/AvalancheMicroscopic.hh"
21 #include "Garfield/TrackHeed.hh"
22 #include "Garfield/ViewDrift.hh"
23 #include "Garfield/ViewSignal.hh"
24
25 using namespace std;
26 using namespace Garfield;
27
28 int main(int argc, char * argv[]) {
29
```

```
30    TApplication app("app", &argc, argv);
31
32  // Define materials
33  // Gas mixture
34    MediumMagboltz *gas = new MediumMagboltz();
35    const double pressure = 760.;
36    const double temperature = 293.15;
37    gas->SetTemperature(temperature);
38    gas->SetPressure(pressure);
39    gas->SetComposition("Ar", 80., "CO2", 20.);
40    gas->LoadGasFile("../ar_80_co2_20_80k.gas");
41
42
43  // Read the ion mobility table from file.
44    const string garfpath = getenv("GARFIELD_HOME");
45    gas->LoadIonMobility(garfpath +
        ↪ "/Data/IonMobility_Ar+_Ar.txt");
46
47  // Other mediums
48    MediumConductor Cu;
49    MediumPlastic kp;
50    kp.SetDielectricConstant(3.9);
51
52  // Geometry.
53    GeometrySimple geo;
54    geo.SetMedium(gas);
55
56    double i_dia = 0.027;
57    double o_dia = 1.9;
58    double length = 15;
59
60    double anode_z = 0.0;
61
62    double cathodeV = 0;
63    double anodeV = 2800;
64    double field = (anodeV-cathodeV)/o_dia;
65
66    double offset = 0.01;
67
68    /*SolidHole tube(0.0, 0.0, 0.0, o_dia/2, o_dia/2,
        ↪ o_dia/2 + offset, o_dia/2 + offset, length/2);
```

```
69  tube.SetBoundaryPotential(cathodeV);
70  geo.AddSolid(&tube, &Cu);*/
71
72  SolidBox box1(o_dia/2, 0.0, 0.0, offset,
      ↪ o_dia/2-offset, length/2);
73  box1.SetBoundaryPotential(cathodeV);
74  geo.AddSolid(&box1, &Cu);
75
76  SolidBox box2(-o_dia/2, 0.0, 0.0, offset,
      ↪ o_dia/2-offset, length/2);
77  box2.SetBoundaryPotential(cathodeV);
78  geo.AddSolid(&box2, &Cu);
79
80  SolidBox box3(0.0, o_dia/2, 0.0, o_dia/2, offset,
      ↪ length/2);
81  box3.SetBoundaryPotential(cathodeV);
82  geo.AddSolid(&box3, &Cu);
83
84  SolidBox box4(0.0, -o_dia/2, 0.0, o_dia/2, offset,
      ↪ length/2);
85  box4.SetBoundaryPotential(cathodeV);
86  geo.AddSolid(&box4, &Cu);
87
88  SolidTube wire(0.0, 0.0, 0.0, i_dia/2, length/2, 0.0,
      ↪ 0.0, 1.0);
89  wire.SetBoundaryPotential(anodeV);
90  wire.SetLabel("anode");
91  geo.AddSolid(&wire, &Cu);
92
93  //=====================================================
94
95
96  // Plot device geometry in 3D
97  /*ViewGeometry geomView;
98  geomView.SetGeometry(&geo);
99  geomView.Plot();
100 app.Run();    // Keep this on to interact with the 3D
      ↪ figure
101 */
102
103 // Plot device geometry in 2D
```

```
104   /*
105   ViewGeometry geomView2d;
106   geomView2d.SetGeometsry(&geo);
107   geomView2d.SetArea(-length, -o_dia, -o_dia, length,
        ↪ o_dia, o_dia);
108   geomView2d.SetPlane(0, -1, 0, 0, 0, 0.0);
109   geomView2d.Plot2d();
110   */
111
112   double tgtElSize = 5.e-3; // target element size -3
113   int minEl = 3, maxEl = 8; // minimum and maximum number
        ↪ of elements 3,11
114   int xcopy = 0, ycopy = 0, zcopy = 0;  // no. of copies
        ↪ in the 3 directions
115   ComponentNeBem3d nebem;
116   nebem.SetGeometry(&geo);
117   nebem.SetNumberOfThreads(8);  // Set no. of threads for
        ↪ the calculation
118   nebem.SetTargetElementSize(tgtElSize);
119   nebem.SetMinMaxNumberOfElements(minEl, maxEl);
120   nebem.UseLUInversion();
121   //nebem.EnableDebugging();
122   nebem.Initialise();
123
124
125   int plot_field = 0; // Plot the electric
        ↪ field/potentials
126   int calc_field = 0; // Store the electric
        ↪ field/potential values in a file
127   int plot_drift_and_signal = 0; // Plot the drift lines
        ↪ of electrons
128   int gain_calc = 1; // Calculate gain of the detector
129
130
131   if(plot_field==1){
132     std::cout<<"\n Potential plotting calculations have
          ↪ begun."<<endl;
133
134     ViewField fieldp;
135     fieldp.SetComponent(&nebem);
```

```
136     fieldp.PlotProfile(0.0, 0.0, 0.0, o_dia/1.8, 0.0,
          ↪ 0.0, "e", false);
137
138     ViewField fieldView;
139     fieldView.SetComponent(&nebem);
140     fieldView.SetNumberOfContours(100);
141     // Set the normal vector of the viewing plane (xz
          ↪ plane).
142     fieldView.SetPlane(0, -1, 0, 0.0, 0.0, 0.0);
143     // Set the plot limits in the current viewing plane.
144     fieldView.SetArea(-length/4, -2*o_dia, length/4,
          ↪ 2*o_dia);
145     //fieldView.SetVoltageRange(-80000., 80000.);
146     TCanvas* cf = new TCanvas("cf", "Potential Plot
          ↪ (V/cm)", 600, 500);
147     //cf->SetLeftMargin(0.16);
148     fieldView.SetCanvas(cf);
149     fieldView.PlotContour("e");
150     char name0[1024];
151     sprintf(name0, "Box_tube_Potential_Plot.pdf");
152     cf->SaveAs(name0);
153   }
154
155   if(calc_field==1){
156     std::cout<<"\n Field calculations have begun."<<endl;
157     {// field along line 1
158     std::ofstream fldfile;
159     char name1[1024];
160     sprintf(name1, "Box_tube_(%d, %d)_along_z.csv",
          ↪ (int)anodeV, (int)cathodeV);
161
162     fldfile.open(name1);
163
164     int nx = 1000;
165     double delx = (o_dia/1.8) / (double)(nx - 1);
166     double xp = 0.0, yp = 0.0, zp = 0.0;
167     Medium* medium = nullptr;
168     double ex = 0., ey = 0., ez = 0., e = 0.0, v = 0.;
169     int status = 0;
170     for(int ix = 0; ix < nx; ++ix){
171       xp = 0.0 + ix*delx;
```

```
172         nebem.ElectricField(xp, yp, zp, ex, ey, ez, v,
                ↪ medium, status);
173         e = (ex*ex + ey*ey + ez*ez);
174         e = pow(e, 0.5);
175         fldfile << xp << "," << yp << "," << zp << "," <<
                ↪ ex << "," << ey << "," << ez << "," << e <<
                ↪ "," << v << "," << medium << "," << status <<
                ↪ std::endl;
176       }
177       fldfile.close();
178       }
179     }
180
181
182     if(plot_drift_and_signal == 1){
183
184        // Create the sensor.
185       Sensor* sensor = new Sensor();
186       sensor->AddComponent(&nebem);
187       double xmax = o_dia/2, ymax = o_dia/2, zmax =
                ↪ length/4, xmin = -o_dia/2, ymin = -o_dia/2, zmin
                ↪ = -length/4;
188       sensor->SetArea(xmax, ymax, zmax, xmin, ymin, zmin);
189       sensor->AddElectrode(&nebem, "anode");
190       std::cout << "Sensor has been created \n";
191
192       // Create the charge multiplication method
193       AvalancheMC* avalMC = new AvalancheMC();
194       avalMC->SetSensor(sensor);
195       //avalMC->EnableAvalancheSizeLimit();
196       avalMC->SetDistanceSteps(); // Use lower value for
                ↪ better precision
197       //avalMC->EnableSignalCalculation();
198
199       // HEED
200       TrackHeed* track = new TrackHeed();
201       track->SetSensor(sensor);
202       track->EnableElectricField();
203       track->SetParticle("mu");   // Incident particle
204       track->SetKineticEnergy(1.0e9); // Kinetic energy of
                ↪ the particle in eV
```

```
205
206     ViewDrift* driftView = new ViewDrift();
207     driftView->SetArea(xmax, ymax, zmax, xmin, ymin,
          ↪ zmin);
208     driftView->SetPlane(0., -1., 0., 0.0, 0.0, 0.0);
209     avalMC->EnablePlotting(driftView);
210     track->EnablePlotting(driftView);
211     TCanvas* cd = new TCanvas();
212     driftView->SetCanvas(cd);
213
214     const double tMin = 0.; // in ns
215     const double tMax = 100.;   // in ns
216     const double tStep = 0.05;  // in ns
217     const int nTimeBins = int((tMax - tMin) / tStep);
218     sensor->SetTimeWindow(tMin, tStep, nTimeBins);
219
220     float time[nTimeBins], current[nTimeBins];
221
222     // The initial position of the incoming ionising track
223     double track_x = o_dia/2.5;
224     double track_y = 0.0;
225     double track_z = 0.0;
226
227     double t0 = 0;
228     double e0 = 0.1;
229     // Momentum direction of incoming track
230     float track_dx = -1.0;
231     float track_dy = 0.0;
232     float track_dz = 0.0;
233
234     int nEvent=1;
235
236     // Cluster info
237     double xcls, ycls, zcls, tcls, ecls, extra;
238     unsigned int ne, ni; // number of electrons in cluster
239     int nel, nend=0;
240     // Electron info
241     double xele, yele, zele, tele, eele, dxele, dyele,
          ↪ dzele;
242     int clust_id;
243
```

```
244     cout<<"\n\nMedium at mid-drift gap ("<<o_dia/3<<"):
           ↪ "<<geo.GetMedium(0.0, 0.0, o_dia/3)<<endl<<endl;
245
246     for(Int_t iEvent=0; iEvent<nEvent;iEvent++){
247       sensor->ClearSignal();     // Reset signals and free
             ↪ the sensor
248       track->NewTrack(track_x, track_y, track_z, tMin,
             ↪ track_dx, track_dy, track_dz);   // Incident
             ↪ particle track
249       bool clust_present=0;
250       clust_id = 0;
251       int p = 0;
252       do{   // Loop over all the cluster positions along
             ↪ the track
253         cout<<"Event = "<<iEvent+1<<": "<<"Cluster =
             ↪ "<<clust_id+1<<" :"<<endl;
254         clust_present=track->GetCluster(xcls, ycls, zcls,
             ↪ tcls, nel, ecls, extra);
255         p = p + nel;
256         for(int j = 0; j < nel; j++){   // Loop over all
             ↪ electrons in a cluster
257           track->GetElectron(j, xele, yele, zele, tele,
               ↪ eele, dxele, dyele, dzele);
258           avalMC->AvalancheElectron(xele, yele, zele,
               ↪ tele);
259           cout<<"\t j= "<<j+1<<"/"<<nel<<endl;
260         }
261         constexpr bool twod = true;
262         driftView->Plot(0);
263         //driftView->Plot(1);
264         //cd->Modified();
265         clust_id++;
266       }while(clust_present!=0);
267
268       int end=avalMC->GetNumberOfElectronEndpoints();
269       cout<<"\n Gain = "<<end<<endl;
270       cd->SaveAs("driftLines.pdf");
271       //driftView->Clear();
272     }
273   }
274
```

```
275   if(gain_calc == 1){
276     double xmin = -o_dia/2, ymin = -o_dia/2, zmin =
          ↪ -length/4;
277     double xmax = o_dia/2, ymax = o_dia/2, zmax =
          ↪ length/4;
278     // Create the sensor.
279     Sensor* sensor = new Sensor();
280     sensor->AddComponent(&nebem);
281     sensor->SetArea(xmax, ymax, zmax, xmin, ymin, zmin);
282     //sensor->AddElectrode(&nebem, "anode");
283     //sensor->AddElectrode(&nebem, "anode2");
284     std::cout << "Sensor has been created \n";
285
286     // Create the charge multiplication method
287     AvalancheMC* avalMC = new AvalancheMC();
288     avalMC->SetSensor(sensor);
289     //avalMC->EnableAvalancheSizeLimit(150);
290     //avalMC->SetDistanceSteps();   // Use lower value
          ↪ for better precision
291     //avalMC->EnableSignalCalculation();
292
293     // The initial position of the incoming ionising track
294     double track_x = o_dia/2.1;
295     double track_y = 0.0;
296     double track_z = 0.0;
297
298     double t0 = 0;
299     double e0 = 0.1;
300     // Momentum direction of incoming track
301     float track_dx = -1.0;
302     float track_dy = 0.0;
303     float track_dz = 0.0;
304
305     int nEvent=1000;
306
307     // Cluster info
308     double xcls, ycls, zcls, tcls, ecls, extra;
309     unsigned int ne, ni; // number of electrons in cluster
310     int nend=0;
311     // Electron info
```

```
312     double xele, yele, zele, tele, eele, dxele, dyele,
           ↪ dzele;
313     int clust_id;
314
315     std::ofstream file;
316     char gain_file[1024];
317     sprintf(gain_file, "Box_tube_gain_%fcm.csv", track_x);
318     file.open(gain_file);
319
320     for(Int_t iEvent=0; iEvent<nEvent;iEvent++){
321       avalMC->AvalancheElectron(track_x, track_y,
             ↪ track_z, t0, false);
322       ne = 0;
323       ni = 0;
324       avalMC->GetAvalancheSize(ne, ni);
325       nend = avalMC->GetNumberOfElectronEndpoints();
326       std::cout<<"\n\nEvent: "<<iEvent+1;
327       std::cout<<"\n\nGain from GetAvalSize(): "<<ne;
328       std::cout<<"\n\nGain from GetNo.ofEndPoints():
             ↪ "<<nend<<endl<<endl;
329       file << iEvent+1 << "," << ne << "," << nend <<
             ↪ std::endl;
330     }
331     file.close();
332   }
333
334   cout<<"\n\n :: Complete :: \n\n";
335   app.Run();
336   return 0;
337 }
```

Bibliography

[1] Ibrahim Alsamak et al. *Garfield++*. URL: https://garfieldpp.web.cern.ch/garfieldpp/.

[2] Tutor L. Benussi. *GEM detector construction and characterization*. INFN, Frascati, Italy, Oct. 2015. URL: https://agenda.infn.it/event/9123/contributions/77376/attachments/56136/66279/EDIT2015Benussi.pdf.

[3] Stephen Biagi. *Magboltz - transport of electrons in gas mixtures*. URL: https://magboltz.web.cern.ch/magboltz/.

[4] Andrew Boston. *Pulse Processing: Pulse Shaping*. URL: https://ns.ph.liv.ac.uk/~ajb/ukgs_nis/pre-course-material/lec2-03.pdf.

[5] A. Breskin et al. "A concise review on THGEM detectors". In: *Nuclear Instruments and Methods in Physics Research Section A: Accelerators, Spectrometers, Detectors and Associated Equipment* 598.1 (2009). Instrumentation for Colliding Beam Physics, pp. 107–111. ISSN: 0168-9002. DOI: https://doi.org/10.1016/j.nima.2008.08.062. URL: https://www.sciencedirect.com/science/article/pii/S0168900208012047.

[6] S Bressler et al. "Recent advances with THGEM detectors". In: *Journal of Instrumentation* 8.12 (Dec. 2013), pp. C12012–C12012. ISSN: 1748-0221. DOI: 10.1088/1748-0221/8/12/c12012. URL: http://dx.doi.org/10.1088/1748-0221/8/12/C12012.

[7] M.A. Chefdeville. "Development of micromegas-like gaseous detectors using a pixel readout chip as collecting anode". Undefined. PhD thesis. University of Amsterdam, Jan. 2009. ISBN: not assigned.

[8] *COMSOL Multiphysics Simulation Software*. URL: https://www.comsol.com/comsol-multiphysics.

[9] Theopisti Dafni. "A Search for Solar Axions with the MICROMEGAS Detector in CAST". PhD thesis. Darmstadt, Tech. U., Oct. 2008.

[10] *Elmer FEM, open source multiphysical simulation software*. URL: http://www.elmerfem.org/blog/.

[11] S.S. Kapoor and V.S. Ramamurthy. *Nuclear Radiation Detectors*. New Age International Publishers, 1986. ISBN: 9780852264966. URL: https://books.google.co.in/books?id=RX5Xdo030X0C.

[12] William R. Leo. *Techniques for Nuclear and Particle Physics Experiments: A How-to Approach*. 2nd. Springer, 1994. ISBN: 3540572805,9783540572800.

[13] John H. Moore et al. *Building Scientific Apparatus*. 4th ed. Cambridge University Press, 2009. ISBN: 0521878586,9780521878586.

[14] Supratik Mukhopadhay and Nayana Majumdar. *A nearly exact Boundary Element Method*. URL: http://nebem.web.cern.ch/nebem/.

[15] *Preamplifier Introduction*. URL: https://www.ortec-online.com/-/media/ametekortec/other/preamplifier-introduction.pdf.

[16] F. Sauli. "GEM: A new concept for electron amplification in gas detectors". In: *Nuclear Instruments and Methods in Physics Research Section A: Accelerators, Spectrometers, Detectors and Associated Equipment* 386.2 (1997), pp. 531–534. ISSN: 0168-9002. DOI: https://doi.org/10.1016/S0168-9002(96)01172-2. URL: https://www.sciencedirect.com/science/article/pii/S0168900296011722.

[17] Fabio Sauli. *Gaseous Radiation Detectors: Fundamentals and Applications*. Cambridge Monographs on Particle Physics, Nuclear Physics and Cosmology. Cambridge University Press, 2014. DOI: 10.1017/CBO9781107337701.

[18] Moritz Seidel. "Microscopic Simulation of GEM Signals". PhD thesis. RWTH Aachen University, Aug. 2018. URL: https://web.physik.rwth-aachen.de/~hebbeker/theses/seidel_bachelor.pdf.

[19] I. B. Smirnov. "Modeling of ionization produced by fast charged particles in gases". In: *Nucl. Instrum. Meth. A* 554 (2005), pp. 474–493. DOI: 10.1016/j.nima.2005.08.064.

[20] *Technical Information Manual MOD. N968 Spectroscopy Amplifier*. URL: https://www.caen.it/products/n968/.

[21] AN Zheng-Hua et al. *Experimental study on the performance of a single-THGEM gas detector*. 2010. DOI: 10.1088/1674-1137/34/1/015. URL: http://hepnp.ihep.ac.cn//article/id/b539b7ac-61f5-4e38-9627-6ed91572ee8f.

[22] James F. Ziegler. *SRIM - The Stopping and Range of Ions in Matter*. URL: http://www.srim.org/.

[23] P. A. Zyla et al. "Review of Particle Physics". In: *PTEP* 2020.8 (2020), p. 083C01. DOI: 10.1093/ptep/ptaa104.